Asymptotic-preserving method for the vorticity equation

Baptiste Fedele[1], Claudia Negulescu[1], and Maurizio Ottaviani[2]

[1]Institut de Mathématiques de Toulouse, Université Paul-Sabatier, Toulouse, France.
[2]CEA Cadarache, Saint-Paul-lez-Durance, France.

October 22, 2019

Abstract

We present an *Asymptotic-Preserving* method to solve numerically the two-dimensional vorticity-Poisson (Navier-Stokes) system. The main focus is the validation of the numerical scheme. As test cases we consider the unforced evolution of Taylor-Green vortices and the forced Kolmogorov flow with a sinusoidal source term. The scheme is validated by comparing the results with those obtained with an explicit spectral code and with an analytic result about the linear instability regime. We show that the AP-properties of the method allow one to deal efficiently with the multi-scale nature of the problem by tuning the time step to the physics one aims to study and not by stability constraints. As a side result, we investigate the long time scale evolution of the Kolmogorov flow, observing that it evolves into a final stable stationary state characterised by a seemingly universal relation between stream-function and vorticity.

Keywords : Asymptotic-Preserving schemes ; Hydrodynamic instabilities ; Singularly perturbed problem.

1 Motivation, background and objectives

The scope of this paper is to present an efficient numerical method to deal with a class of problems coming from incompressible fluid mechanics, of which the paradigm is the two-dimensional vorticity equation:

$$(\mathcal{V})^\epsilon \quad \begin{cases} \partial_t \omega^\epsilon + \dfrac{1}{\epsilon}\mathbf{u}^\epsilon \cdot \nabla \omega^\epsilon = (\Delta \omega^\epsilon - \Delta \omega_{eq}), \quad (t,\mathbf{x}) \in \mathbb{R}^+ \times \Omega, \\ -\Delta \Psi^\epsilon = \omega^\epsilon, \qquad \mathbf{u}^\epsilon = {}^\perp \nabla \Psi^\epsilon, \quad (t,\mathbf{x}) \in \mathbb{R}^+ \times \Omega, \end{cases} \tag{1.1}$$

where $\mathbf{x} := (x, y) \in \Omega$ with Ω an open, bounded domain of $\mathbb{R}^2$, in our case a rectangle. The problem is complemented by periodic boundary conditions and it consists

of an evolution equation for the vorticity ω^ϵ, coupled to the Poisson equation for the computation of the stream-function Ψ^ϵ. This latter function is fixed by imposing the constraint $\langle \Psi^\epsilon \rangle = 0$ where $\langle \cdot \rangle$ denotes the average over the domain Ω . The perpendicular gradient operator is defined as ${}^\perp\nabla := (\partial_y, -\partial_x)$. The parameter $\epsilon \in (0,1)$ models the stiffness of the problem, and its physical significance will be explained in Section 1.1. The term ω_{eq} appearing on the right hand side of system (1.1) denotes a forcing term. In this paper, we examine two well-known vortex-problems: the Taylor-Green flow (unforced case $\omega_{eq}(\mathbf{x}) = 0$) and the Kolmogorov flow (forced case $\omega_{eq}(\mathbf{x}) = \cos(x)$), with special emphasis on the stability properties of these flows. The study of such simple flows is precious, as it helps to acquire intuition and insight by displaying the particular behavior of the flow under the influence of different physical mechanisms and also by providing ideal test cases for checking numerical methods. Our main focus will be the numerical investigation of the instability of equilibria-flows described by (1.1), and this via an *Asymptotic-Preserving scheme* [12,13]. In particular, we are interested in the validation of the proposed AP-scheme, which was especially designed to capture efficiently and accurately all ϵ-regimes, notably the $\epsilon \to 0$ limit regime.

In this work we restrict the study to 2D flows. This is done primarily for practical reasons, while developing and validating the scheme. There is however a practical interest about flows occurring in Nature that exhibit 2D dynamics, such as those found in geophysical, astrophysical and oceanographic context. These flows are subject to strong geometrical constraints, so that the vertical motion can be often neglected (hurricanes, the Great Red Spot of Jupiter, the vortex Gulf Stream, etc.). We refer the interested reader to [14] for a review of vortex dynamics in Nature. In the context of magnetised plasma physics, such quasi-2D flows can occur as a consequence of the strong magnetic field which induces a strongly anisotropic dynamics. The earliest model equation was derived by [10]. It describes the evolution of the electric potential in a plane perpendicular to the magnetic field and it is only slightly more general than the model studied in the present work.

The Taylor-Green flow is a particular 2D vortex flow, which evolves from a single-Fourier mode initial condition (for ex. $\omega_{in} = 2 \sin x \sin y$), without forcing ($\omega_{eq}(\mathbf{x}) = 0$). The analytic solution is known in this case and will be considered as the time-dependent equilibrium-solution to be perturbed. Without perturbation the initial vortices are damped in time by dissipation, while keeping the same shape. It is however well-known, that this solution is unstable, giving rise, when perturbed, to mixing processes or filamentation, leading eventually to a state with a completely reconfigured final flow. The Taylor-Green flow can be considered as a model of the Von Karman flow such as the one depicted in figure 1, panel (a).
The Kolmogorov flow corresponds to a 2D, one-directional shear flow, with sinusoidal velocity profile, which is maintained by a forcing term ($\omega_{eq}(\mathbf{x}) = \cos(x)$), in the presence of viscosity. It admits a stationary solution, the laminar Kolmogorov flow, which can be unstable under certain conditions. One then observes the emergence of complex time-dependent structures, leading first to a characteristic island pattern (also sometimes called cat's eye), then, as the systems evolves, to a complete rearrangement of the flow, leading to a stationary end state. The Kolmogorov flow can

be considered as a paradigm of a channel flow without boundaries such as the one sketched in figure 1, panel (b).

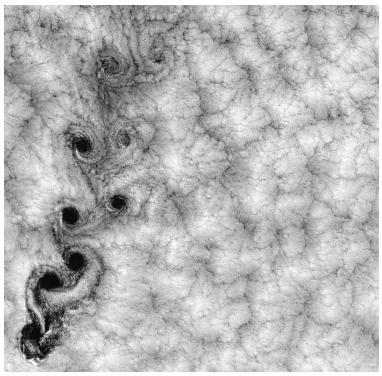

(a) Von Karman flow.

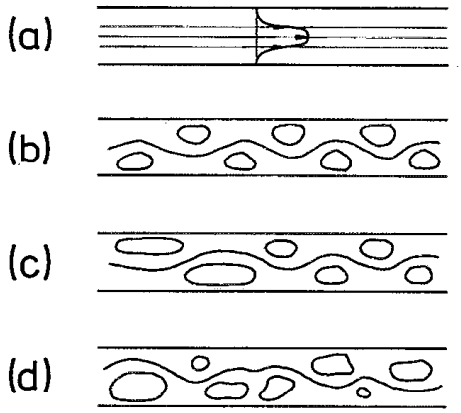

(b) Channel flow.

Figure 1: Two examples of flow, representing respectively the Von Karman flow (a) and a channel flow (b).

Studying the instability of shear flows is a notorious numerically difficult problem. Indeed, the occurrence of several time and space scales (eddies with a wide range of sizes), as well as the sensitivity of the solution (unstable equilibria) to numerical errors, make numerical integration delicate. In particular, if one is interested in capturing long-time asymptotics, efficient numerical schemes are needed, allowing one to control the accumulation of the errors over the time. Simulation methods that do not pay sufficient attention to these issues are likely to fail. Numerical strategies must take full advantage of the asymptotic properties of the underlying problem in order to be efficient. In view of all these difficulties, our present aim is to introduce and validate an *Asymptotic-Preserving method*, which allows one to overcome the above mentioned complications. In particular, such a scheme should be able to reach directly the equilibrium state (when it exists), skipping the intermediate states, and as a consequence, avoiding the error accumulation. Moreover, by exploiting the asymptotics of the problem at hand, the scheme can largely reduce the computational time when one is interested in the large time scale dynamics.

In the rest of this work, we rewrite the system $(\mathcal{V})^\epsilon$ as :

$$(\mathcal{V})^\epsilon \quad \begin{cases} \partial_t \omega^\epsilon + \dfrac{1}{\epsilon}\{\omega^\epsilon, \Psi^\epsilon\} = (\Delta \omega^\epsilon - \Delta \omega_{eq}), \quad (t, \mathbf{x}) \in \mathbb{R}^+ \times \Omega, \\ -\Delta \Psi^\epsilon = \omega^\epsilon, \quad (t, \mathbf{x}) \in \mathbb{R}^+ \times \Omega, \end{cases} \tag{1.2}$$

where $\{\omega^\epsilon, \Psi^\epsilon\} = \partial_x \omega^\epsilon \, \partial_y \Psi^\epsilon - \partial_y \omega^\epsilon \, \partial_x \Psi^\epsilon$ denotes the Poisson bracket. This form is more adequate for simulations, as we will discretise the Poisson bracket with the *Arakawa scheme* [2], which was devised specifically for such an advection term.

The outline of this paper is the following. In the remaining of Section 1, the physical origin of system (1.1) is briefly reviewed, its multiscale nature is highlighted and some useful quantities are introduced. Section 2 deals with the Asymptotic-Preserving reformulation of our original problem (1.1) in order to obtain a more regular problem. This reformulation is based on a Micro-Macro decomposition of the unknown variable, and it is completed by a regularization procedure. The second part of Section 2 presents the numerical scheme that we develop in this paper. Section 3 focuses on the numerical study of the Taylor-Green test case. The main purpose of this Section is to validate our numerical procedure. Section 4 is dedicated to the study of the Kolmogorov flow. An analytic result about the relation between the growth rate of the linear instability of this flow and the aspect ratio of the domain is given. Furthermore, the nonlinear instability phase as well as the final state of the Kolmogorov flow are investigated. In particular, we find a functional relation between the stream function and the vorticity in the final state the numerical solution obtained by our numerical procedure. This article ends with Section 5 where some conclusions and perspectives are given.

1.1 Non-dimensional Vorticity-Poisson system

Our study is based on the incompressible Navier-Stokes equations, which describes a bi-dimensional flow with velocity $\mathbf{u} := (u_x, u_y, 0)^T$, pressure p and forcing term $\mathbf{u}_{eq}$:

$$(\mathcal{NS}) \begin{cases} \partial_t \mathbf{u} + (\mathbf{u}\cdot\nabla)\mathbf{u} = -\nabla p + \nu(\Delta\mathbf{u} - \Delta\mathbf{u}_{eq}), \quad (t,\mathbf{x}) \in \mathbb{R}^+ \times \Omega, \\ \nabla\cdot\mathbf{u} = 0, \quad (t,\mathbf{x}) \in \mathbb{R}^+ \times \Omega, \end{cases} \tag{1.3}$$

where ν denotes the kinematic viscosity of the fluid. The divergence-free constraint of $\mathbf{u}$ leads to the existence of a scalar stream-function Ψ such that $\mathbf{u} =^{\perp} \nabla\Psi = (\partial_y\Psi, -\partial_x\Psi, 0)^T$. Introducing the vorticity $\omega = (\nabla\times\mathbf{u})\cdot\mathbf{e_z}$, we take the curl of (1.3) and then the scalar product with $\mathbf{e_z} := (0,0,1)^T$, to rewrite this system in the equivalent vorticity/stream-function form

$$(\mathcal{V}) \begin{cases} \partial_t \omega + \{\omega, \Psi\} = \nu(\Delta\omega - \Delta\omega_{eq}), \quad (t,\mathbf{x}) \in \mathbb{R}^+ \times \Omega, \\ -\Delta\Psi = \omega, \quad (t,\mathbf{x}) \in \mathbb{R}^+ \times \Omega. \end{cases} \tag{1.4}$$

In this work, we will consider different time scales. It is therefore useful to proceed with non-dimensional equations to identify the regimes of interest. For each function generically denoted by $n(\cdot)$, we set $n(\cdot) := \bar{n}\, n'(\cdot)$, where $\bar{n}$ refers to the characteristic scale of $n(\cdot)$ and n' the non-dimensional associated function. With these notations, we now fix the spatial and time characteristic lengths $\bar{x}$ and $\bar{t}$ of the flow. Starting from the pair $(\bar{x}, \bar{t})$, we deduce the characteristic scales of the other quantities:

$$\bar{u} = \frac{\bar{x}}{\bar{t}}, \quad \bar{\omega} = \frac{\bar{u}}{\bar{x}}, \quad \bar{\Psi} = \bar{x}\,\bar{u}.$$

Replacing in the vorticity problem (1.4) each quantity $n(\cdot)$ by $\bar{n}\, n'$, we obtain

$$(\mathcal{V})\ \begin{cases} \partial_{t'}\omega' + \{\omega', \Psi'\} = \dfrac{\nu\,\bar{t}}{\bar{x}^2}(\Delta\omega' - \Delta\omega'_{eq}), \quad (t', \mathbf{x}) \in \mathbb{R}^+ \times \Omega\,, \\ -\Delta\Psi' = \omega', \quad (t', \mathbf{x}) \in \mathbb{R}^+ \times \Omega\,. \end{cases} \tag{1.5}$$

Introducing now a viscous time scale $\tau_\nu := \dfrac{\bar{x}^2}{\nu}$, the previous system can be written

$$(\mathcal{V})\ \begin{cases} \partial_{t'}\omega' + \{\omega', \Psi'\} = \dfrac{\bar{t}}{\tau_\nu}(\Delta\omega' - \Delta\omega'_{eq}), \quad (t', \mathbf{x}) \in \mathbb{R}^+ \times \Omega\,, \\ -\Delta\Psi' = \omega', \quad (t', \mathbf{x}) \in \mathbb{R}^+ \times \Omega\,. \end{cases} \tag{1.6}$$

Supposing that the viscous time scale τ_ν is very long compared to the observation time scale $\bar{t}$, we introduce the stiffness parameter ϵ standing for this ratio:

$$\epsilon := \frac{\bar{t}}{\tau_\nu} \in (0, 1).$$

If we are now interested in describing phenomena arising on non-viscous time scales, the vorticity model can be written as

$$(\mathcal{V})\ \begin{cases} \partial_{t'}\omega + \{\omega, \Psi\} = \epsilon\,(\Delta\omega - \Delta\omega_{eq}), \quad t' \in (0, \mathcal{T}), \\ -\Delta\Psi = \omega\,, \end{cases} \tag{1.7}$$

with $\mathcal{T} \in \mathbb{R}^+$ a fixed final time. On the other hand, if we are interested in characterizing phenomena arising on the viscous time scale, we set $t = \epsilon\,t'$, and the Vorticity-Poisson system can be written as

$$(\mathcal{V})^\epsilon\ \begin{cases} \partial_t\omega^\epsilon + \dfrac{1}{\epsilon}\{\omega^\epsilon, \Psi^\epsilon\} = (\Delta\omega^\epsilon - \Delta\omega_{eq}), \quad t \in (0, T), \\ -\Delta\Psi^\epsilon = \omega^\epsilon\,. \end{cases} \tag{1.8}$$

with T linked to $\mathcal{T}$ by the relation $T = \epsilon\,\mathcal{T}$. This is the starting point of our investigations.

1.2 Some quantities of interest

We recall here the definition of some integral quantities that will be used in our study. In the following, $|\Omega|$ denotes the measure of the domain Ω.

The kinetic energy $\mathcal{K}^\epsilon(t, \omega^\epsilon)$, enstrophy $\mathcal{E}^\epsilon(t, \omega^\epsilon)$ and palinstrophy $\mathcal{P}^\epsilon(t, \omega^\epsilon)$ are defined respectively by

$$\mathcal{K}^\epsilon(t, \omega^\epsilon) = \frac{1}{2|\Omega|}\int_\Omega \Psi^\epsilon(t, x, y)\,\omega^\epsilon(t, x, y)\,\mathrm{d}x\,\mathrm{d}y = \frac{1}{2|\Omega|}\int_\Omega |\mathbf{u}^\epsilon(t, x, y)|^2\mathrm{d}x\,\mathrm{d}y.$$

$$\mathcal{E}^\epsilon(t, \omega^\epsilon) = \frac{1}{2|\Omega|}\int_\Omega [\omega^\epsilon(t, x, y)]^2\mathrm{d}x\,\mathrm{d}y,$$

$$\mathcal{P}^\epsilon(t,\omega^\epsilon) = \frac{1}{2|\Omega|}\int_\Omega [\nabla\omega^\epsilon(t,x,y)]^2 \mathrm{d}x\,\mathrm{d}y.$$

The time evolution of the kinetic energy is given by the relation

$$\frac{\mathrm{d}}{\mathrm{d}t}\mathcal{K}^\epsilon(t,\omega) = -2\left(\mathcal{E}^\epsilon(t,\omega) + I^\epsilon(t,\mathbf{u})\right),$$

where $I^\epsilon(t,\mathbf{u}^\epsilon) = \dfrac{1}{2|\Omega|}\displaystyle\int_\Omega \Delta\,\mathbf{u}_{eq}\cdot\mathbf{u}^\epsilon\,\mathrm{d}x\,\mathrm{d}y$ denotes the input energy through the external forcing velocity $\mathbf{u}_{eq}$.

The time evolution of the enstrophy satisfies

$$\frac{\mathrm{d}}{\mathrm{d}t}\mathcal{E}^\epsilon(t,\omega^\epsilon) = -2\left(\mathcal{P}^\epsilon(t,\omega^\epsilon) + J^\epsilon(t,\omega^\epsilon)\right),$$

where $J^\epsilon(t,\omega^\epsilon) = \dfrac{1}{2|\Omega|}\displaystyle\int_\Omega \Delta\,\omega_{eq}\,\omega^\epsilon\,\mathrm{d}x\,\mathrm{d}y$ describes the enstrophy production through the external forcing ω_{eq}.
We observe that the kinetic energy and the enstrophy decrease in time when the forcing term is zero.

We also introduce two quantities, the Rayleigh quotient $\mathcal{R}^\epsilon(t,\omega^\epsilon)$, and the dissipation quotient $\Lambda^\epsilon(t,\omega^\epsilon)$:

$$\mathcal{R}^\epsilon(t,\omega^\epsilon) = \frac{\mathcal{E}^\epsilon(t,\omega^\epsilon)}{\mathcal{K}^\epsilon(t,\omega^\epsilon)}, \qquad \Lambda^\epsilon(t,\omega^\epsilon) = \frac{\mathcal{P}^\epsilon(t,\omega^\epsilon)}{\mathcal{E}^\epsilon(t,\omega^\epsilon)}.$$

The time derivative of the Rayleigh quotient verifies the following relation, obtained after simple computations

$$\frac{\mathrm{d}}{\mathrm{d}t}\mathcal{R}^\epsilon(t,\omega^\epsilon) = -2\,\mathcal{R}^\epsilon(t,\omega^\epsilon)\left[\Lambda^\epsilon(t,\omega^\epsilon) - \mathcal{R}^\epsilon(t,\omega^\epsilon) + \mathcal{K}^\epsilon(t,\omega^\epsilon)\left(J^\epsilon(t,\omega^\epsilon)/\mathcal{R}^\epsilon(t,\omega^\epsilon)\right.\right.$$

$$\left.\left. - I^\epsilon(t,\mathbf{u}^\epsilon)\right)\right].$$

2 Numerical scheme

In this section we describe the numerical scheme we have developed for an efficient resolution of (1.1). We start by carrying out an Asymptotic-Preserving reformulation of the model. We then make use of the Arakawa scheme for the advection operators as well as the Diagonal Implicit Runge-Kutta (DIRK) approach for the time derivative.

2.1 Asymptotic-Preserving reformulation

An Asymptotic-Preserving scheme is a numerical approach designed to solve efficiently singularly-perturbed problems, denoted generically P^ϵ, which contain some small parameter $\epsilon \in [0,1]$. A precise definition of an AP-scheme is given in the next definition (see also commutative diagram in figure 2).

Definition 2.1 *Consider a singularly-perturbed problem P^ϵ, whose solution is assumed to converge (in a certain sense) towards the solution of a limit problem P^0. An AP-scheme for P^ϵ, denoted $P^{\epsilon,\mathbf{h}}$, is a numerical scheme which enjoys the following properties:*

- *The AP-scheme $P^{\epsilon,\mathbf{h}}$ is stable in a suitable sense, uniformly in ϵ.*
- *For fixed stiffness parameter $\epsilon > 0$, the AP-scheme $P^{\epsilon,\mathbf{h}}$ provides a consistent discretization of the problem P^ϵ, as $\mathbf{h} \to 0$.*
- *For fixed discretization parameters $\mathbf{h} > 0$, the AP-scheme $P^{\epsilon,\mathbf{h}}$ provides in the limit $\epsilon \to 0$ a consistent discretization of the limit problem P^0.*

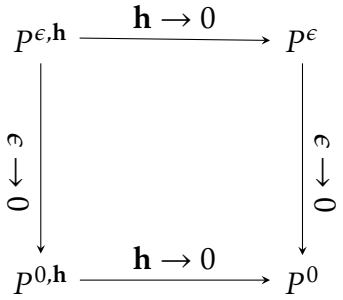

Figure 2: Commutative properties of AP-schemes.

Physical problems arising in nature are complex and contain several time and space scales, which are difficult to capture in their globality with standard schemes. Classical numerical procedures such as explicit methods are submitted to a CFL-condition, which forces the user to solve also the small scales of the problem, which can be sometimes undesirable. This leads necessarily to huge computational costs. Fully implicit methods can sometimes suffer from accuracy problems when the perturbation parameter is too small, as they do not capture the asymptotic limit. In such multi-scale frameworks, AP-schemes become interesting, as they allow eliminating those scales which are not relevant in the considered study without loosing accuracy and without stability problems. This aspect will be illustrated in the last part of this work.

The AP-reformulation we shall introduce for the resolution of (1.8) is based on the following decomposition of the vorticity field ω^ϵ into a macroscopic and a microscopic part, namely

$$\omega^\epsilon = \chi^\epsilon + \epsilon\, \xi^\epsilon\,, \tag{2.9}$$

where χ^ϵ denotes the macroscopic part, which belongs to the kernel of the dominant transport operator $\mathcal{T}_{\Psi^\epsilon} := \{\cdot, \Psi^\epsilon\}$ and ξ^ϵ denotes the microscopic part.
Inserting now (2.9) in (1.8), allows one to obtain the following system for the unknowns $(\omega^\epsilon, \xi^\epsilon, \Psi^\epsilon)$:

$$(\mathcal{MM})^{\epsilon}\begin{cases} \partial_t \omega^{\epsilon} + \{\xi^{\epsilon}, \Psi^{\epsilon}\} = (\Delta \omega^{\epsilon} - \Delta \omega_{eq}), \quad (t,\mathbf{x}) \in (0,T)\times\Omega\,, \\ \{\omega^{\epsilon}, \Psi^{\epsilon}\} - \epsilon\{\xi^{\epsilon}, \Psi^{\epsilon}\} = 0\,, \quad (t,\mathbf{x}) \in (0,T)\times\Omega\,, \\ -\Delta\Psi^{\epsilon} = \omega^{\epsilon}\,, \quad (t,\mathbf{x}) \in (0,T)\times\Omega\,. \end{cases} \tag{2.10}$$

This reformulation of (1.8) is now a regular problem in ϵ, allowing one to capture for $\epsilon \to 0$ the limit problem $(\mathcal{MM})^0$. Nevertheless, it is ill-posed since ξ^{ϵ} is not unique. To overcome this new problem, we shall employ a regularization technique already proposed in [7], by inserting the term $\sigma\,\xi^{\epsilon}$ in the second equation of (2.10). We obtain then the final reformulated system:

$$(\mathcal{MM})^{\epsilon}_{\sigma}\begin{cases} \partial_t \omega^{\epsilon,\sigma} + \{\xi^{\epsilon,\sigma}, \Psi^{\epsilon,\sigma}\} = (\Delta \omega^{\epsilon,\sigma} - \Delta \omega_{eq}), \quad (t,\mathbf{x}) \in (0,T)\times\Omega\,, \\ \{\omega^{\epsilon,\sigma}, \Psi^{\epsilon,\sigma}\} - \epsilon\{\xi^{\epsilon,\sigma}, \Psi^{\epsilon,\sigma}\} + \sigma\,\xi^{\epsilon,\sigma} = 0\,, \quad (t,\mathbf{x}) \in (0,T)\times\Omega\,, \\ -\Delta\Psi^{\epsilon,\sigma} = \omega^{\epsilon,\sigma}\,, \quad (t,\mathbf{x}) \in (0,T)\times\Omega\,. \end{cases} \tag{2.11}$$

Note that due to the regularization, $(\mathcal{MM})^{\epsilon}_{\sigma}$ is no more equivalent to $(\mathcal{MM})^{\epsilon}$, however σ shall be chosen small enough, of the order of the truncation error, in order not to modify too much the initial problem.

2.2 Numerical discretization

We hereby describe in detail the numerical discretization of the reformulated system (2.11).

2.2.1 Discretisation parameters

In what follows, we consider a bounded simulation domain $\Omega_S := (0,L_x)\times(0,L_y)$ and all considered functions are supposed to be doubly periodic in x and y. The time interval $[0,T]$, $T>0$, is discretized as follows :

$$t^n := n\Delta t\,, \quad \Delta t := T/N_t\,, \quad n \in [\![0,N_t]\!], \quad N_t \in \mathbb{N}.$$

In order to provide a uniform mesh on the domain Ω_S, we define the grid spacings as follow :

$$x_i := (i-1)\Delta x\,, \quad y_j := (j-1)\Delta y\,, \quad \Delta x := L_x/N_x\,, \quad \Delta y := L_y/N_y\,,$$

where $i \in [\![1,N_x+1]\!]$, and $j \in [\![1,N_y+1]\!]$. For any function $f : [0,T]\times\Omega_S \to \mathbb{R}$, $f^n_{i,j}$ refers to the numerical approximation of $f(t^n,x_i,y_j)$, and f^n_h shall denote the discrete grid-function $(f^n_{i,j})_{i,j}$. Because of periodic boundary conditions, we set :

$$f^n_{N_x+1,j} = f^n_{1,j}\,, \quad f^n_{i,N_y+1} = f^n_{i,1}\,, \quad \forall (n,i,j) \in [\![0,N_t]\!] \times [\![1,N_x+1]\!] \times [\![1,N_y+1]\!].$$

2.2.2 Space semi-discretisation

Let us proceed with the discretisation of the operators appearing in (2.11). For the discrete Laplace operator evaluated at the point (x_i, y_j), one has

$$[\Delta_h f_h]_{i,j} := \frac{1}{\Delta x^2}(f_{i+1,j} - 2f_{i,j} + f_{i-1,j}) + \frac{1}{\Delta y^2}(f_{i,j+1} - 2f_{i,j} + f_{i,j-1}).$$

For the Poisson brackets operator, let us use the second order Arakawa discretisation [2]. For two functions $f, g : \Omega_S \to \mathbb{R}$, the discrete version of the Poisson bracket $\{f, g\}$ evaluated at the point (x_i, y_j) is expressed by :

$$[f_h, g_h]_{i,j} := \frac{1}{12\Delta x\Delta y}\Big(f_{i+1,j}\,\mathcal{A}_{i,j} + f_{i-1,j}\,\mathcal{B}_{i,j} + f_{i,j+1}\,\mathcal{C}_{i,j} + f_{i,j-1}\,\mathcal{D}_{i,j}$$
$$+ f_{i+1,j+1}\,\mathcal{E}_{i,j} + f_{i-1,j-1}\,\mathcal{F}_{i,j} + f_{i-1,j+1}\,\mathcal{G}_{i,j} + f_{i+1,j-1}\,\mathcal{H}_{i,j}\Big).$$

where the coefficients write

$$\mathcal{A}_{i,j} := g_{i,j+1} - g_{i,j-1} + g_{i+1,j+1} - g_{i+1,j-1}, \qquad \mathcal{E}_{i,j} := g_{i,j+1} - g_{i+1,j},$$
$$\mathcal{B}_{i,j} := g_{i,j-1} - g_{i,j+1} - g_{i-1,j+1} + g_{i-1,j-1}, \qquad \mathcal{F}_{i,j} := g_{i,j-1} - g_{i-1,j},$$
$$\mathcal{C}_{i,j} := g_{i-1,j} - g_{i+1,j} - g_{i+1,j+1} + g_{i-1,j+1}, \qquad \mathcal{G}_{i,j} := g_{i-1,j} - g_{i,j+1},$$
$$\mathcal{D}_{i,j} := g_{i+1,j} - g_{i-1,j} + g_{i+1,j-1} - g_{i-1,j-1}, \qquad \mathcal{H}_{i,j} := g_{i+1,j} - g_{i,j-1}.$$

We finish this paragraph with the discretisation of the Poisson equation $-\Delta f = g$. In order to limit the computational cost of the scheme, we resolve this latter by the Fourier method. For a discrete grid-function $(f_{i,j})_{i,j}$, we denote by $(\widehat{f_{p,q}})_{p,q}$ its discrete Fourier transform, where $p \in [\![-N_x/2, N_x/2]\!]$ and $q \in [\![-N_y/2, N_y/2]\!]$. Introducing the quantities

$$k_p = \frac{2\pi p}{L_x}, \quad k_q = \frac{2\pi q}{L_y},$$

the Poisson equation $-\Delta f = g$ becomes, after the application of the discrete Fourier transform,

$$\widehat{f_{p,q}} = \frac{\widehat{g_{p,q}}}{k_p^2 + k_q^2}.$$

And denoting by $\widetilde{f}$ the inverse discrete Fourier transform of f, we obtain

$$(f_{i,j})_{i,j} = \widetilde{(\widehat{f_{p,q}})_{p,q}}.$$

2.2.3 Time discretisation

In order to achieve second-order accuracy in time for the problem (2.11), we use a Diagonally Implicit Runge Kutta (DIRK) approach. The Runge-Kutta (RK) method is recalled here for clarity reasons [1].

We consider a problem of the form $\partial_t f = L(f) + g(t)$, where L denotes some differential operator and g a source term. An r-stage Runge-Kutta approach is characterized by its Butcher table

$$\begin{array}{c|ccc} c_1 & a_{11} & \dots & a_{1r} \\ \vdots & \vdots & & \vdots \\ c_r & a_{r1} & \dots & a_{rr} \\ \hline & b_1 & \dots & b_r \end{array} .$$

For a given u^n, the subsequent u^{n+1} is defined by the formula

$$u^{n+1} = u^n + \Delta t \sum_{j=1}^{r} b_j \left(L(u_j) + g(t + c_j \Delta t)\right),$$

where each u_i is defined by

$$u_i = u^n + \Delta t \sum_{j=1}^{r} a_{i,j} (L(u_j) + g(t + c_j \Delta t)).$$

Note that in the case where $b_j = a_{rj}$ for $j = 1, ..., r$, then u^{n+1} is equal to the last stage of the method, namely u_r. For our problem (2.11), we consider the following 2-stage Butcher table

$$\begin{array}{c|cc} \mu & \mu & 0 \\ 1 & 1-\mu & \mu \\ \hline & 1-\mu & \mu \end{array} .$$

In all our simulations, we choose $\mu := 1 - 1/\sqrt{2}$. With this choice, the method is $L-stable$ [**?**, see]Sec. IV-3]ger.

2.2.4 Fixed point procedure and final scheme

Due to the nonlinearity of our problem (2.11), in particular the fact that the function $\Psi^{\epsilon,\sigma}$ is linked to the function $\omega^{\epsilon,\sigma}$ via the Poisson equation, we have to develop a fixed point procedure in order to resolve numerically the problem (2.11) with an implicit numerical method. If we choose $l \in \mathbb{N}$ as an iteration index, the stream-function $\Psi^{\epsilon,\sigma}$ can be considered as fixed during the iteration step $l \to l+1$, given by the previous iteration. We denote by $\Delta t^\star$ the product $\mu \Delta t$.

For each time step $n \in \mathbb{N}$, we are looking thus for $(\omega_h^{\epsilon,\sigma,n+1}, \xi_h^{\epsilon,\sigma,n+1})$, by iterating in $l \in \mathbb{N}$ as follows.
Starting from

$$\omega_{i,j}^{\epsilon,\sigma,n+1,0} := \omega_{i,j}^{\epsilon,\sigma,n}, \quad \text{we have}$$

$$\begin{cases} \textbf{Poisson solver:} \\ \widehat{\Psi_{p,q}^{\epsilon,\sigma,n+1},l} = \dfrac{\widehat{\omega_{p,q}^{\epsilon,\sigma,n+1},l}}{k_p^2 + k_q^2}. \\ \textbf{Stage 1:} \\ \omega_{1,i,j}^{\epsilon,\sigma,n+1,l+1} + \Delta t^\star [\xi_{1,h}^{\epsilon,\sigma,n+1,l+1}, \Psi_h^{\epsilon,\sigma,n+1,l}]_{i,j} = \omega_{i,j}^{\epsilon,\sigma,n} + \Delta t^\star \Big(\Big[\Delta \omega_{1,h}^{\epsilon,\sigma,n+1,l+1}\Big]_{i,j} \\ -\Big[\Delta \omega_{eq,h}\Big]_{i,j}\Big), \\ [\omega_{1,h}^{\epsilon,\sigma,n+1,l+1}, \Psi_h^{\epsilon,\sigma,n+1,l}]_{i,j} - \epsilon [\xi_{1,h}^{\epsilon,\sigma,n+1,l+1}, \Psi_h^{\epsilon,\sigma,n+1,l}]_{i,j} + \sigma\, \xi_{1,i,j}^{\epsilon,\sigma,n+1,l+1} = 0. \\ \textbf{Stage 2:} \\ \omega_{2,i,j}^{\epsilon,\sigma,n+1,l+1} + \Delta t^\star [\xi_{2,h}^{\epsilon,\sigma,n+1,l+1}, \Psi_h^{\epsilon,\sigma,n+1,l}]_{i,j} = \omega_{i,j}^{\epsilon,\sigma,n} + \dfrac{1-\mu}{\mu}(\omega_{1,i,j}^{\epsilon,\sigma,n+1,l+1} - \omega_{i,j}^{\epsilon,\sigma,n}) \\ +\Delta t^\star \Big(\Big[\Delta \omega_{2,h}^{\epsilon,\sigma,n+1,l+1}\Big]_{i,j} - \Big[\Delta \omega_{eq,h}\Big]_{i,j}\Big), \\ [\omega_{2,h}^{\epsilon,\sigma,n+1,l+1}, \Psi_h^{\epsilon,\sigma,n+1,l}]_{i,j} - \epsilon [\xi_{2,h}^{\epsilon,\sigma,n+1,l+1}, \Psi_h^{\epsilon,\sigma,n+1,l}]_{i,j} + \sigma\, \xi_{2,i,j}^{\epsilon,\sigma,n+1,l+1} = 0. \\ \textbf{Final stage:} \\ (\omega_{i,j}^{\epsilon,\sigma,n+1,l+1}, \xi_{i,j}^{\epsilon,\sigma,n+1,l+1}) = (\omega_{2,i,j}^{\epsilon,\sigma,n+1,l+1}, \xi_{2,i,j}^{\epsilon,\sigma,n+1,l+1}). \end{cases} \tag{2.12}$$

In all of the subsequent simulations, the stopping criterion chosen for these iterations (at $l = l_f$) is

$$\frac{\Big| \|\omega_h^{\epsilon,\sigma,n+1,l+1}\|_{L_h^1} - \|\omega_h^{\epsilon,\sigma,n+1,l}\|_{L_h^1} \Big|}{\|\omega_h^{\epsilon,\sigma,n+1,l}\|_{L_h^1}} + \frac{\Big| \|\Psi_h^{\epsilon,\sigma,n+1,l+1}\|_{L_h^1} - \|\Psi_h^{\epsilon,\sigma,n+1,l}\|_{L_h^1} \Big|}{\|\Psi_h^{\epsilon,\sigma,n+1,l}\|_{L_h^1}} < 10^{-2},$$

where $\|f_h\|_{L_h^1} := \Delta x \Delta y \sum_{i=1}^{N_x+1} \sum_{j=1}^{N_y+1} |f_{i,j}|$ denotes the discrete L_1- norm of a grid function f_h. We end the procedure by setting

$$\omega_{i,j}^{\epsilon,\sigma,n+1} := \omega_{i,j}^{\epsilon,\sigma,n+1,l_f+1},$$
$$\xi_{i,j}^{\epsilon,\sigma,n+1} := \xi_{i,j}^{\epsilon,\sigma,n+1,l_f+1}.$$

Finally, the new stream-function at iteration $n+1$ is computed then via

$$(\Psi_{i,j}^{\epsilon,\sigma,n+1})_{i,j} = (\widetilde{\widehat{\Psi_{p,q}^{\epsilon,\sigma,n+1}}})_{p,q}, \quad \text{with} \quad \widehat{\Psi_{p,q}^{\epsilon,\sigma,n+1}} := \frac{\widehat{\omega_{p,q}^{\epsilon,\sigma,n+1}}}{k_p^2 + k_q^2}.$$

We refer to the scheme developed in this section as (DAMM)-scheme for Dirk-Arakawa-Micro-Macro (scheme).

3 Numerical study of the Taylor-Green vortex case

The aim of this section is to validate the (DAMM)-scheme with a classic benchmark, the Taylor-Green flow, without forcing: $\omega_{eq} \equiv 0$.

The Taylor-Green flow is a known analytic solution of the system (1.8). This flow is characterized by a periodic array of counter-rotating vortices decaying in time. In the following, we choose the box domain $\Omega_S = (0, L_x) \times (0, L_y)$, with $L_x = L_y = 2\pi$, associated with periodic boundary conditions. At the initial time, $t = 0$, we consider the vorticity field $\omega_{in}^A(x, y) = 2\sin(x)\sin(y)$. This leads to the following exact solution of the vorticity equation (1.8) $\omega^{ex}(t, x, y) = 2\exp(-2t)\sin(x)\sin(y)$, which corresponds to a velocity field of $\mathbf{u}^{ex}(t, x, y) = \exp(-2t)(\cos(y)\sin(x), -\cos(x)\sin(y))^T$, and a stream-function $\Psi_{ex}(t, x, y) = \exp(-2t)\sin(x)\sin(y)$. Thus, at later times, the solution has the same flow pattern but with decreasing amplitude because of the viscous dissipation. In particular, since the stream-function is proportional to the vorticity field in that case, the Poisson bracket $\frac{1}{\epsilon}\{\omega^{ex}, \Psi^{ex}\}$ vanishes at all times.

3.1 The Taylor-Green vortex for large values of ϵ.

Before starting the simulations, we recall that we denote by $\mathcal{T}$ the physical time and by T the simulation one. These two times are linked by the relation : $T = \epsilon\mathcal{T}$. Let us first validate the damping rate of the Taylor-Green vortices. The initial condition ω_{in}^A was introduced just before. In figure 3 (a), we plot a cut of the solution $\omega^{\epsilon,\sigma}$ at $y = \pi/4$ obtained with the (DAMM)-scheme (2.12) at three physical times : $t = 0$, $t = \mathcal{T}/2$ and $t = \mathcal{T}$, with $\mathcal{T} = 1$ and $\epsilon = 1$ (remark that in this case, $t = t'$ and $T = \mathcal{T}$). Moreover, we superpose the analytical solution ω^{ex} at the same times. We observe a perfect correspondence between the two solutions, for the considered times. The dissipation of the vortices caused by the viscosity is moreover clearly visible. In figure 3 (b), we plot the evolution in time of the vorticity maximum, obtained with the (DAMM)-scheme for two values of ϵ, namely $\epsilon = 1$ and $\epsilon = 0.1$ and $\mathcal{T} = 1$. As expected, the dissipation is stronger for higher ϵ. As before, we include in figure 3 (b) the analytic solution. The correspondence between the two solutions is clearly visible, allowing one to confirm that the (DAMM)-scheme reproduces the expected behaviour of the flow in this case.

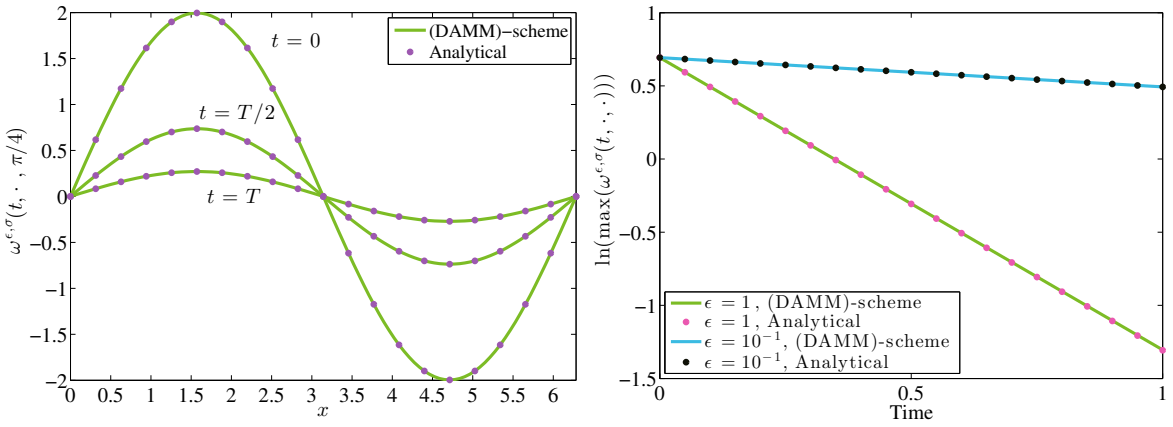

(a) (b)

Figure 3: (Taylor-Green vortex solution for large ϵ-values and initial condition ω_{in}^{A}). Cut at $y = \pi/4$ of the vorticity field versus x at three different times (a). Evolution in time of the vorticity maximum for two different values of ϵ : $\epsilon = 1$ and $\epsilon = 0.1$ (b). Parameters were $N_x = N_y = 100$, $\Delta t = 0.001$, $\mathcal{T} = 1$ and $\sigma = (\Delta x/L_x)^2$.

We now show that the (DAMM)-scheme verifies the relations established earlier about the kinetic energy, the enstrophy, and the palinstrophy. For this, we have plotted in figure 4 (a) the evolution in time of these quantities, for $\epsilon = 1$. We observe the decrease towards zero of all these quantities, as expected, since the flow is viscously damped. Furthermore, the link between the time derivative of the kinetic energy and the enstrophy, as well as the link between the time derivative of the enstrophy and the palinstrophy is also well-reproduced by the (DAMM)-scheme. In figure 4 (b), we plot the enstrophy as a function of the kinetic energy. There is clearly a linear relation between the two quantities, which indicates that the Rayleigh quotient is constant over time. Moreover, if we plot the evolution of $\Lambda(\omega^{\epsilon,\sigma})$ as a function of the kinetic energy, we find the same straight line, thus $\Lambda^{\epsilon,\sigma}(\omega^{\epsilon,\sigma}) = \mathcal{R}^{\epsilon,\sigma}(\omega^{\epsilon,\sigma}) = cte$, meaning the relation connecting $\mathcal{R}^{\epsilon,\sigma}$, $\dfrac{\mathrm{d}}{\mathrm{d}t}\mathcal{R}^{\epsilon,\sigma}$ and $\Lambda^{\epsilon,\sigma}$ is also verified by the (DAMM)-scheme.

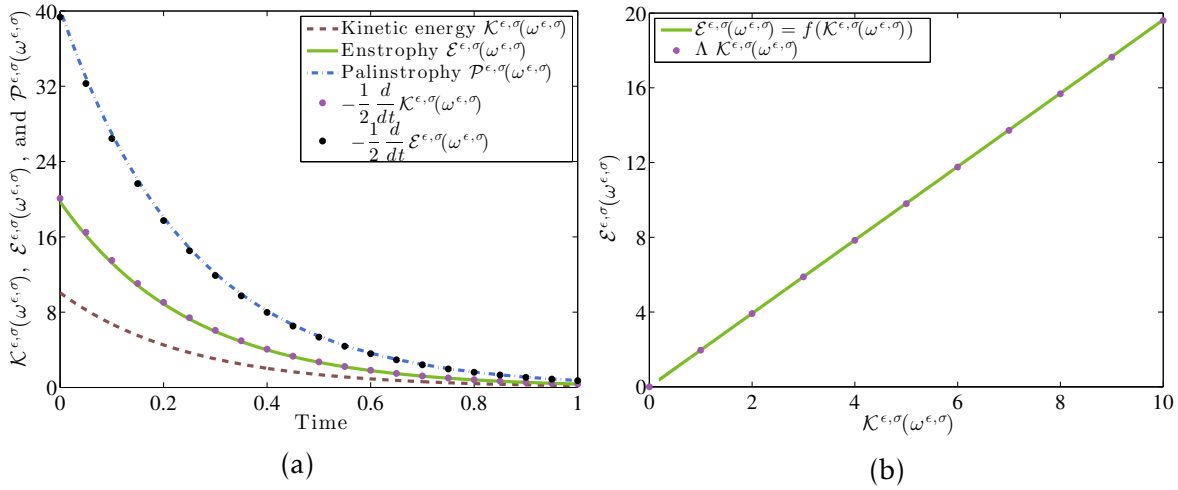

Figure 4: (Taylor-Green vortex for $\epsilon = 1$, with initial condition ω_{in}^{A}). Evolution in time of the kinetic energy, enstrophy, palinstrophy, and time derivatives of the kinetic energy and enstrophy (a) ; Kinetic energy-enstrophy diagram showing that the Rayleigh quotient is constant over time (b). Parameters were $N_x = N_y = 100$, $\Delta t = 0.001$, $\mathcal{T} = 1$, $\sigma = (\Delta x/L_x)^2$.

As a second test, we perturb the initial condition as follows $\omega_{in}^{B} = \omega_{in}^{A} + \beta\,\mathcal{N}(x,y)$, where $\beta = 0.1$ and $\mathcal{N}(x,y)$ represents a noise in the form of a random value between 0 and 1, at each point (x,y). Due to this noise, the Poisson bracket $\{\omega^{\epsilon,\sigma}, \Psi^{\epsilon,\sigma}\}$ is no longer zero and the symmetry of the initial vorticity field is broken. In figure 5, we plot the vorticity field $\omega^{\epsilon,\sigma}$ at different times, obtained with the (DAMM)-scheme from the noisy initial condition ω_{in}^{B}. Starting from four perturbed counter-rotating vortices (a), we observe this time the beginning of an instability and of the movement of the vortices (b). Then, a filamentation of the vortices (c), and a wavy pattern of the two occuring stripes appears (d). Vorticity is stretched and compressed by the flow, a known effect related to the enstrophy cascade. Finally, the flow begins to stabilize (e), and to approach a two-stripe pattern (f), although no equilibrium seems to be attained at this time. This sequence of figures shows a classical aspect of turbulence in the two dimensional case, *i.e.* the appearance of coherent structures embedded in the filamentation picture. Here the initial characteristic length of the vorticity patch is $L = \pi$ and attains 2π at the final time. This instability was recently studied in [20] where similar figures were obtained, with a different numerical scheme, namely a high accuracy compact scheme on a non-uniform grid coupled with a fourth-order Runge-Kutta method.

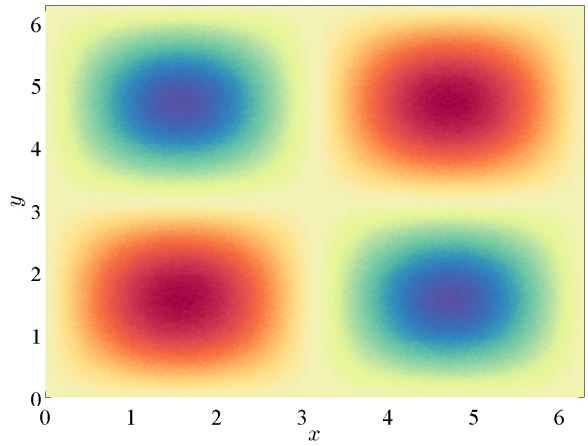

(a) (DAMM)-scheme, $n = 0$.

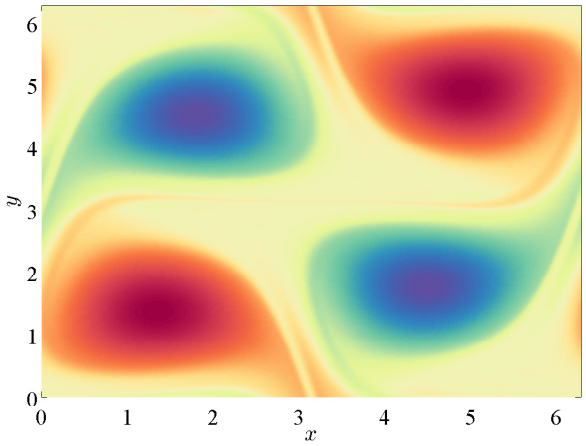

(b) (DAMM)-scheme, $n = 1100$.

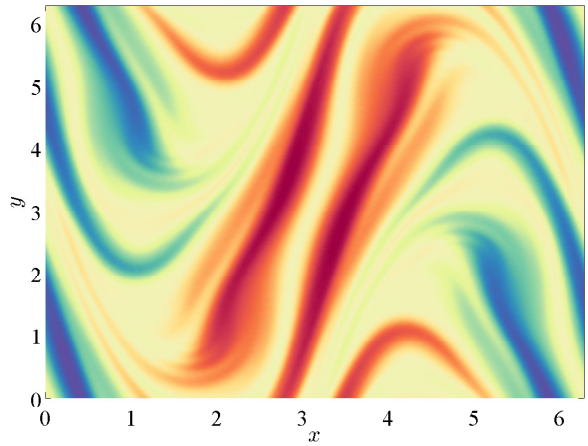

(c) (DAMM)-scheme, $n = 1350$.

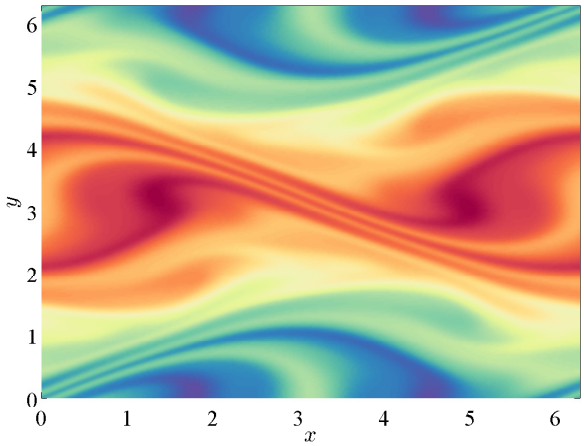

(d) (DAMM)-scheme, $n = 1900$.

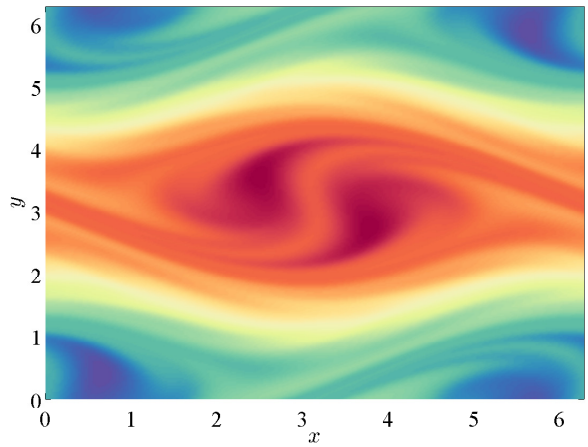

(e) (DAMM)-scheme, $n = 2250$.

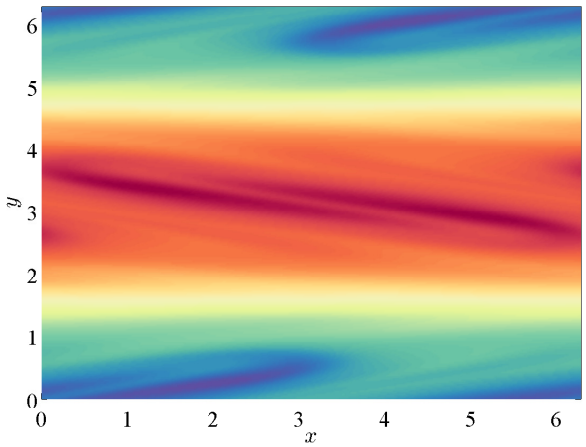

(f) (DAMM)-scheme, $n = 2500$.

Figure 5: (Taylor-Green vortex with initial condition ω_{in}^{B}). Vorticity field $\omega^{\epsilon,\sigma}$ at different times. Parameters were $\epsilon = 5e-4$, $N_x = N_y = 256$, $N_t = 2500$, $\mathcal{T} = 150$, and $\sigma = (\Delta x/L_x)^2$.

As we did previously for the non-perturbed Taylor-Green flow, we investigate now the evolution of the quantities of interest. In figure 6 (a), we plot the evolution of the kinetic energy and of the enstrophy. One sees that due to the viscosity, the enstrophy and the kinetic energy decay in time, as expected. However, in figure 6 (b) we observe several large peaks of the palinstrophy around the physical times of $t' = 75$ and $t' = 85$. These kind of bursts correspond to the merging of the likely-colored vortices, merging during which the gradient of the vorticity is locally maximal. As expected, the sudden increase of palinstrophy from $t' \approx 70$ to $t' \approx 115$, corresponding to the filamentation and the merging phases of vortices, coincides with the maximal decrease phases of both enstrophy and kinetic energy.

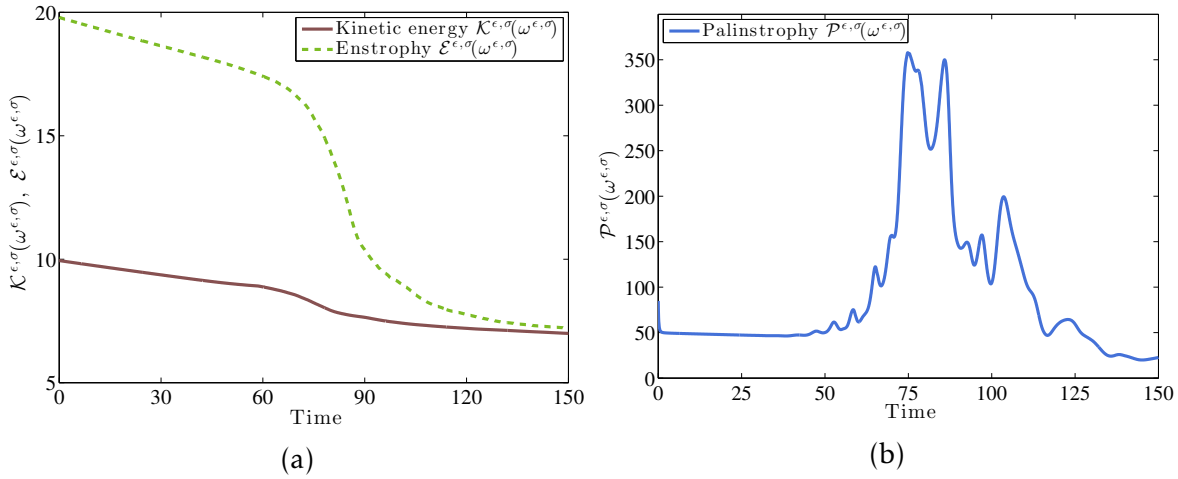

Figure 6: (Taylor-Green vortex with initial condition ω_{in}^{B}). Evolution over time of kinetic energy and enstrophy (a), and of the palinstrophy (b). Parameters were $\epsilon = 5e-4$, $N_x = N_y = 256$, $N_t = 2500$, $\mathcal{T} = 150$, and $\sigma = (\Delta x/L_x)^2$.

This first test case allowed us to validate our numerical procedure. Indeed, the (DAMM)-scheme is able to recover the multiple relations linking several physical quantities of interest like the kinetic energy, the enstrophy, the palinstrophy and so on. Moreover, we could reproduce the unstable flow occurring when the initial conditions of the Taylor-Green flow are perturbed. In the next section we focus one the Kolmogorov flow, in order to investigate the viscous-time asymptotics $\epsilon \to 0$ in a forced case.

4 Study of a forced case - Kolmogorov flow

In this section we apply our numerical scheme to the forced version of (1.1). The primary scope is to validate the scheme when applied to a multiple time scale situation with a non trivial final state (in the previous study, the final state at infinite time is one without flow). As we will see, in our case, the short time scale associated with the linear instability of the initial equilibrium is inertial, whereas the long (infinite) time steady state is achieved on the viscous time scale. In the following, we first carry

out a stability study, both analytically and numerically, of the unstable equilibrium determined by a particular choice of the forcing term. We then carry out a study of the nonlinear evolution for long times, taking advantage of the capability of the AP scheme to employ time steps that are tuned to the physics under study. Finally, the validation of the AP scheme is supported also by a comparison with the results of the solution obtained with a spectral method, showing also the advantage of the former on the latter. As an interesting results, the final state at infinite time shows universal features, whose origin is however still a matter of investigation.

As a forcing term we choose the simple form $\omega_{eq}(x,y) = \cos(x)$ and as a domain we take a flat torus $\Omega = (-\pi,\pi) \times \left(-\frac{\pi}{K}, \frac{\pi}{K} \right)$, where $1/K \in \mathbb{R}^+$ denotes the aspect ratio. We associate to (1.1) periodic boundary conditions for both vorticity and stream-function. The system (1.1) rewrites then

$$(\mathcal{K})^\epsilon \quad \begin{cases} \partial_t \omega^\epsilon + \dfrac{1}{\epsilon} \mathbf{u}^\epsilon \cdot \nabla \omega^\epsilon = (\Delta \omega^\epsilon + \cos(x)), \quad (t,\mathbf{x}) \in \mathbb{R}^+ \times \Omega \,, \\ -\Delta \Psi^\epsilon = \omega^\epsilon \,, \qquad \mathbf{u}^\epsilon = ^\perp \nabla \Psi^\epsilon \,, \quad (t,\mathbf{x}) \in \mathbb{R}^+ \times \Omega \,. \end{cases} \tag{4.13}$$

It is trivial to see that $\omega^\epsilon \equiv \omega_{eq}$ is a steady-state solution, also called equilibrium or fixed point, of this system. This equilibrium is linearly unstable under certain conditions which makes the system an interesting test case.

Historically, this flow was introduced by Kolmogorov [3, 4] as a part of his work concerning hydrodynamic stability problems and turbulence, and there exists substantial literature about this problem (4.13). In the following, we are particularly interested in its linear stability, which was first investigated by [16], and then completed by [11]. They prove, using an elegant continuous fraction method, that when $K > 1$ the steady-state solution ω_{eq} is stable. However, when $K < 1$, they show that there exists a critical value of the viscosity below which the solution ω_{eq} becomes unstable. Furthermore, a global stability result was given in [15] for all forcing amplitudes when $K = 1$.

4.1 Linear instability of the Kolmogorov flow

In this subsection, we examine the linear stability properties of (4.13). We first derive approximate solutions of the linear problem, then we verify them numerically.

From the above-cited results in the literature [11,16], one knows that when $0 < K < 1$, there exists a critical value of ϵ , denoted by $\epsilon_\star$, below which an instability appears. Since the linear instability occurs on the short time scale, it is convenient to work with the vorticity equation normalized to the non-viscous time scale:

$$(\mathcal{K}) \quad \begin{cases} \partial_{t'} \omega + \mathbf{u} \cdot \nabla \omega = \epsilon \, (\Delta \omega + \cos(x)), \quad (t',\mathbf{x}) \in \mathbb{R}^+ \times \Omega \,, \\ -\Delta \Psi = \omega \,, \qquad \mathbf{u} = ^\perp \nabla \Psi \,, \quad (t',\mathbf{x}) \in \mathbb{R}^+ \times \Omega \,. \end{cases} \tag{4.14}$$

Let us set $\widetilde{\omega} := \omega - \omega_{eq}$, $\widetilde{\mathbf{u}} := \mathbf{u} - \mathbf{u}_{eq}$ and $\widetilde{\Psi} := \Psi - \Psi_{eq}$, with $\Psi_{eq}(x) = \cos(x)$ and $\mathbf{u}_{eq} = (0, \sin(x))^T$. Reformulating (4.14) in these fluctuating quantities, and neglecting the small terms of order 2, we obtain the linearized system:

$$(L) \begin{cases} \partial_{t'} \widetilde{\omega} + \widetilde{\mathbf{u}} \cdot \nabla \omega_{eq} + \mathbf{u}_{eq} \cdot \nabla \widetilde{\omega} = \epsilon \Delta \widetilde{\omega}, \quad (t', \mathbf{x}) \in \mathbb{R}^+ \times \Omega, \\ -\Delta \widetilde{\Psi} = \widetilde{\omega}, \qquad \widetilde{\mathbf{u}} =^{\perp} \nabla \widetilde{\Psi}, \qquad \mathbf{u}_{eq} =^{\perp} \nabla \Psi_{eq}, \quad (t', \mathbf{x}) \in \mathbb{R}^+ \times \Omega. \end{cases} \tag{4.15}$$

Combining all these equations, we can obtain an equation verified only by $\widetilde{\Psi}$:

$$\partial_{t'} \Delta \widetilde{\Psi} + \sin(x)\, \partial_y (\widetilde{\Psi} + \Delta \widetilde{\Psi}) = \epsilon \Delta^2 \widetilde{\Psi}. \tag{4.16}$$

Because of the homogeneity in time and in the y direction, we can look for a solution of the equation (4.16) in the form $\widetilde{\Psi}(t', x, y) = \widehat{\Psi}(x)\, e^{\gamma t'} e^{\mathrm{i} K y}$, with γ a complex number. Inserting this expression into the previous equation, we obtain an equation for the amplitude function $\widehat{\Psi}$: (we have dropped in the following the hat of $\widehat{\Psi}$ for clarity reasons)

$$\begin{aligned} \gamma\,(\Psi''(x) - K^2 \Psi(x)) + \mathrm{i} K \sin(x)\,(\Psi''(x) + \eta\, \Psi(x)) = & \epsilon\,(\Psi^{(4)}(x) - 2K^2 \Psi''(x) \\ & + K^4 \Psi(x)), \end{aligned} \tag{4.17}$$

with $\eta = 1 - K^2$. The prime denotes the x-derivative.

Eq. (4.17) is a particular case of the Orr-Sommerfeld equation [**?**, see]]drazin, with a sinusoidal velocity profile $U(x) = \sin(x)$.

The general treatment of the spectral problem given by (4.17), which to our knowledge is still unsolved, is outside the scope of this work. Here, we are only interested in finding unstable solutions such that $\mathrm{Re}(\gamma) > 0$. From the previously cited literature, one can argue that for any given small value of ϵ, a critical value of η, denoted by $\eta_\star(\epsilon)$, exists, such that for $\eta > \eta_\star(\epsilon)$, $\mathrm{Re}(\gamma) > 0$. One can further *conjecture* that $\eta_\star(\epsilon)$ tends to zero as ϵ tends to zero. Thus, in this limit, one expects that the instability threshold occurs when the domain aspect ratio is unity.

Note however that, in general, the viscous term constitutes a *singular* perturbation. As a consequence, solutions and eigenvalues depend non trivially on ϵ, the former possessing sharp boundary layers whose width tends to zero as ϵ tends to zero.

In our context, however, namely an unstable case with a simple sinusoidal velocity profile, a preliminary numerical exploration indicates that there exists only one solution with small $\mathrm{Re}(\gamma) > 0$ when $\epsilon \to 0$ and η is small but finite. This solutions is such that the boundary layer is finite. For this class of solutions the viscosity term constitutes a *regular* perturbation. One can then proceed by first dropping the viscosity term, by solving the approximate problem, and then by justifying the procedure

a posteriori. Furthermore one finds that this solution has the property that $\mathrm{Re}(\gamma) \to 0$ when $\eta \to 0$. All this is confirmed by the numerical study as described later.

Neglecting the viscosity term leads to the Rayleigh equation

$$-\mathrm{i}\,\widehat{\gamma}(\Psi''(x) - (1-\eta)\,\Psi(x)) + \sin(x)\,(\Psi''(x) + \eta\,\Psi(x)) = 0\,, \quad x \in (-\pi, \pi)\,, \tag{4.18}$$

where $\widehat{\gamma} := \gamma/K$.

We refer to the book of Drazin & Reid and the references therein for a review of the analysis of equations (4.17)-(4.18) [5]. In particular, the analysis of the Rayleigh equation (4.18) can be viewed as the starting point of the stability study of the shear-flow. Naturally, as the Rayleigh equation is an ODE of order 2, it can provide only an approximation of two solutions of the Orr-Sommerfeld equation (4.17) which admits four independent solutions [5].

We proceed by first noting that when $\sin(x)$ can be considered of order unity, the solution $\Psi(x) = \text{const}$ is sufficiently good. However near $x = 0$ and $x = \pm\pi$, $\sin(x)$ tends to zero and the solution may pick up an appreciable value of $\Psi''(x)$. One therefore expects (internal) boundary layers in the neighbourhood of these points. In figure 7, we have sketched the expected modulus of the solution Ψ of (4.18) which satisfies the boundary conditions.

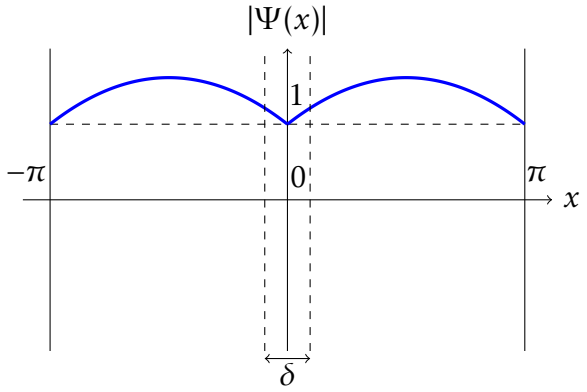

Figure 7: Sketch of the expected modulus of the solution $\Psi(x)$ of (4.18) .

A frequently employed method to deal with boundary value problems is the matched asymptotic expansion method [**?**, see]]VanD,lager,holm for a detailed introduction to these methods). One divides the domain in regions, called the inner and the outer regions. In the outer regions, the variations of the function Ψ are of order 1, so that one can construct solutions in these regions (called the outer solutions) by solving the equation obtained when neglecting the terms of order $\widehat{\gamma}$ and η in (4.18) . In the inner regions, near the boundary layers at $x = 0$ and $x = \pm\pi$, the variations of the function Ψ are very rapid, say of order $1/\widehat{\gamma}^{\,\alpha}$ for some $\alpha > 0$. One looks for corresponding approximate solutions called the inner solution. The method can work if the regions of validity of the inner and of the outer solutions overlap. In these overlapping regions,

one has two asymptotically equivalent solutions which then allow one to derive relations between the arbitrary constants of the solutions of the differential equations in any given region. This matching process can be carried out under the condition that some constraint holds. This constraint constitutes the sought-for relation between the small parameter and the eigenvalue.

We have carried out the above mentioned procedure and the main finding is that solutions can be found if the growth rate $\widehat{\gamma}$ is proportional to η. This is briefly sketched below.

As far as the outer solutions are concerned, one finds that there exists a small number δ, depending on η (so that δ tends to zero when η tends to zero) such that, in the intervals $I_+^\delta = [\delta/2, \pi - \delta/2]$ and $I_-^\delta = [-\pi + \delta/2, -\delta/2]$, the outer solution can be written as

$$\Psi^{\mathbf{O}}(x) = A_+ \left(1 - \frac{\eta}{2}x^2 + \frac{\eta\pi}{2}|x| - \frac{\eta}{2}\left(\frac{\pi}{2}\right)^2 - \mathrm{i}\,\widehat{\gamma}(G(x) + C_1)\right) + \mathcal{R}_+(x,\eta,\delta), \quad x \in I_+^\delta, \quad (4.19)$$

$$\Psi^{\mathbf{O}}(x) = A_- \left(1 - \frac{\eta}{2}x^2 + \frac{\eta\pi}{2}|x| - \frac{\eta}{2}\left(\frac{\pi}{2}\right)^2 - \mathrm{i}\,\widehat{\gamma}(G(x) - C_1)\right) + \mathcal{R}_-(x,\eta,\delta), \quad x \in I_-^\delta, \quad (4.20)$$

where $G(x) = x\ln(|\tan(x/2)|) - 2\int_0^{\tan(x/2)} \frac{\arctan(t)}{t}\,\mathrm{d}t$, $A_\pm$ is a complex constant to be defined and $C_1 = 2\int_0^1 \frac{\arctan(t)}{t}\,\mathrm{d}t$. The terms $\mathcal{R}_+$, $\mathcal{R}_-$ are residual parts of higher order in η.
These solutions were obtained by expanding Ψ in powers of η and assuming symmetry around $x = \pm\pi/2$.

As far as the inner equation is concerned, it is customary to work with a stretched variable. For the equation around $x = 0$, one chooses $\xi = x/\widehat{\gamma}$. By approximating $\sin(x) \approx x$ and introducing further the complex variable $z = 1 + \mathrm{i}\,\xi$, one can write the inner equation in the form:

$$\frac{\mathrm{d}^2\Psi^{\mathbf{I}}}{\mathrm{d}z^2}(z) + \frac{\widehat{\gamma}^2}{z}\Psi^{\mathbf{I}}(z) = 0. \quad (4.21)$$

This equation can be solved in various ways in terms of known functions. As far as asymptotic matching is concerned, to leading order, the simplest way is to expand $\Psi^{\mathbf{I}}$ in powers of $\widehat{\gamma}^2$, with the lowest order solution being a constant. The end result is

$$\Psi^{\mathbf{I}}(\xi) = a + \widehat{\gamma}^2(\mathbf{i}\,b\,\xi - a\,H(\xi)) + \mathcal{R}(\widehat{\gamma},\xi,\Delta), \quad (4.22)$$

in terms of the stretched variable, where a is a real fixed constant, b a complex constant to be determined, $H(\xi) = (1+\mathrm{i}\,\xi)\ln(1+\mathrm{i}\,\xi)$ and $\mathcal{R}$ a residual term of order higher than η^2.

Matching the outer solutions (4.19) for small x with the inner solution (4.21) for large ξ, introduces relations between the various coefficients which imply a constraint between η and $\widehat{\gamma}$:

$$\widehat{\gamma} = \eta\,,$$

to leading order in η.

It is useful to notice that a common feature of both the inner and outer solutions is that, for the problem at hand, both can be derived as an expansion in powers of η and $\widehat{\gamma}$, with the lowest order being a constant. This is consistent with the sketch of figure 7.

This observation suggests a different, more synthetic method to derive the solution of (4.18)*. This is described in detail in the following pages.*

We begin by recasting (4.18) in the form

$$\Psi''(x) = Q(x)\Psi(x)\,, \tag{4.23}$$

where

$$Q(x) = -\eta - \frac{\mathrm{i}\,\widehat{\gamma}}{-\mathrm{i}\,\widehat{\gamma} + \sin(x)}\,. \tag{4.24}$$

Note that $Q(x)$ depends on η and $\widehat{\gamma}$ in such a way that it can be considered as small except in a narrow region around $x = 0$ and $x = \pm\pi$.
To the lowest order in $\widehat{\gamma}$ and η, $\Psi(x)$ is a linear function whose slope must be set to zero in order to satisfy the boundary conditions. $\Psi(0)$ is then a constant which can be fixed to unity in full generality. One can then write:

$$\Psi(x) = 1 + \widetilde{\Phi}(x)\,, \tag{4.25}$$

where $\widetilde{\Phi}(x)$ is a small correction that embodies the dependence on η and $\widehat{\gamma}$. Proceeding iteratively, and neglecting the product $\widetilde{\Phi}(x)Q(x)$ with respect to Q, one obtains

$$\widetilde{\Phi}''(x) = Q(x)\,. \tag{4.26}$$

We start by giving a result which allows one to find the relation between $\widehat{\gamma}$ and η:

Proposition 1 *In order to satisfy the periodic boundary condition* $\widetilde{\Phi}'(\pi) = \widetilde{\Phi}'(-\pi)$*, it is necessary to have*

$$\frac{\widehat{\gamma}}{(1+\widehat{\gamma}^{\,2})^{1/2}} = \eta\,. \tag{4.27}$$

Proof: Integrating once (4.26) gives

$$\widetilde{\Phi}'(x) = \int_0^x Q(x')\,\mathrm{d}x' + C\,. \tag{4.28}$$

Then, the periodic boundary condition $\widetilde{\Phi}'(\pi) = \widetilde{\Phi}'(-\pi)$ requires:

$$\int_{-\pi}^{+\pi} Q(x')\,\mathrm{d}x' = 0\,. \tag{4.29}$$

A primitive of Q can be computed analytically:

$$\int Q(x')\,\mathrm{d}x' = -\eta\,x + \frac{2\,\widehat{\gamma}}{\sqrt{1+\widehat{\gamma}^{\,2}}}\,\arctan\left(\frac{\mathrm{i}+\widehat{\gamma}\tan(x/2)}{\sqrt{1+\widehat{\gamma}^{\,2}}}\right).$$

And then, the constraint (4.29) leads to the desired result. ∎

Note that the relation (4.27) is equivalent to $\widehat{\gamma} \approx \eta$, to leading order in $\widehat{\gamma}$.

Another quantity which allows one to validate our numerical method is the phase difference of the solution between the mid points at $x = \pm\pi/2$ and the reference point $x = 0$, where, by construction, $\Psi(0) = 1$. The phase is given by:

$$\theta_{\pm} = \arctan\left[\frac{\mathrm{Im}(\Psi(\pm\pi/2))}{\mathrm{Re}(\Psi(\pm\pi/2))}\right]. \tag{4.30}$$

Before giving the expression of $\theta_{\pm}$, we state the following Lemma:

Lemma 4.1 *Consider $a > 0$, one has :*

$$\int \frac{x'}{\mathrm{i}\,\sin(x')+a}\,\mathrm{d}x' = \frac{1}{\sqrt{1+a^2}}\left[\mathrm{i}\,x\left(\ln\left(1+\frac{e^{\mathrm{i}\,x}}{a+\sqrt{1+a^2}}\right)-\ln\left(1-\frac{e^{\mathrm{i}\,x}}{a+\sqrt{1+a^2}}\right)\right)\right.$$
$$\left. +\,\mathrm{Li}_2\left(\frac{-e^{\mathrm{i}\,x}}{a+\sqrt{1+a^2}}\right)-\mathrm{Li}_2\left(\frac{e^{\mathrm{i}\,x}}{a+\sqrt{1+a^2}}\right)\right],$$

where Li_2 *denotes the dilogarithm function [21].*

Now, we give the following proposition:

Proposition 2 *To the leading order in $\widehat{\gamma}$, we have :*

$$\theta_{\pm} = \arctan\left[\frac{\mathrm{Im}(\Psi(\pm\pi/2))}{\mathrm{Re}(\Psi(\pm\pi/2))}\right] = \arctan\left(\frac{\pm C_1\,\widehat{\gamma}}{1+\eta\,\pi^2/8}\right) + O(\widehat{\gamma}^{\,2}\ln(\widehat{\gamma})) + O(\widehat{\gamma}^{\,2}),$$

where $C_1 = 2\int_0^1 \frac{\arctan(t)}{t}\,\mathrm{d}t$.

Proof: We compute the values $\widetilde{\Phi}(\pm\pi/2)$ necessary for the computation of $\theta_{\pm}$. By integrating $\widetilde{\Phi}'$, given in (4.28) one has:

$$\widetilde{\Phi}(x) = -\,\eta\,\frac{x^2}{2} + C\,x + \frac{2\,\widehat{\gamma}}{\sqrt{1+\widehat{\gamma}^{\,2}}}\left[\int_0^x \arctan\left(\frac{\mathrm{i}+\widehat{\gamma}\tan(x'/2)}{\sqrt{1+\widehat{\gamma}^{\,2}}}\right)\mathrm{d}x'\right.$$

$$- x \arctan\left(\frac{\mathrm{i}}{\sqrt{1+\widehat{\gamma}^2}}\right)\Bigg] + C_2 .$$

The constant C_2 is equal to 0 since $\widetilde{\Phi}(0) = 0$.

Consider now the primitive of $\arctan\left(\frac{\mathrm{i}+\widehat{\gamma}\tan(x/2)}{\sqrt{1+\widehat{\gamma}^2}}\right)$. By integrating by parts, we obtain:

$$\int \arctan\left(\frac{\mathrm{i}+\widehat{\gamma}\tan(x'/2)}{\sqrt{1+\widehat{\gamma}^2}}\right)\mathrm{d}x' = x \arctan\left(\frac{\mathrm{i}+\widehat{\gamma}\tan(x/2)}{\sqrt{1+\widehat{\gamma}^2}}\right) - \frac{\sqrt{1+\widehat{\gamma}^2}}{2}\int \frac{x'}{\mathrm{i}\sin(x)+\widehat{\gamma}}\mathrm{d}x',$$

and the primitive is obtained from the Lemma 4.2. Thus, the periodic boundary condition $\widetilde{\Phi}(\pi) = \widetilde{\Phi}(-\pi)$ fixes the value of C by:

$$C = \frac{\widehat{\gamma}}{2\pi}\int_{-\pi}^{\pi} \frac{x'}{\mathrm{i}\sin(x')+\widehat{\gamma}}\mathrm{d}x' + \frac{2\widehat{\gamma}}{\sqrt{1+\widehat{\gamma}^2}}\arctan\left(\frac{\mathrm{i}}{\sqrt{1+\widehat{\gamma}^2}}\right).$$

To the leading order in $\widehat{\gamma}$, we have thus

$$C = -\frac{\mathrm{i}\widehat{\gamma}}{\sqrt{1+\widehat{\gamma}^2}}\ln\left(\frac{2}{\widehat{\gamma}}\right) + \frac{2\widehat{\gamma}}{\sqrt{1+\widehat{\gamma}^2}}\arctan\left(\frac{\mathrm{i}}{\sqrt{1+\widehat{\gamma}^2}}\right) + O(\widehat{\gamma}^2).$$

This leads to

$$\widetilde{\Phi}(\pi/2) = -\eta\frac{\pi^2}{8} - \frac{\mathrm{i}\pi\widehat{\gamma}}{2\sqrt{1+\widehat{\gamma}^2}}\ln\left(\frac{2}{\widehat{\gamma}}\right) + \frac{2\widehat{\gamma}}{\sqrt{1+\widehat{\gamma}^2}}\int_0^{\pi/2}\arctan\left(\frac{\mathrm{i}+\widehat{\gamma}\tan(x'/2)}{\sqrt{1+\widehat{\gamma}^2}}\right)\mathrm{d}x' + O(\widehat{\gamma}^2).$$

Now, the integral term can be reformulated as:

$$\frac{2\widehat{\gamma}}{\sqrt{1+\widehat{\gamma}^2}}\int_0^{\pi/2}\arctan\left(\frac{\mathrm{i}+\widehat{\gamma}\tan(x'/2)}{\sqrt{1+\widehat{\gamma}^2}}\right)\mathrm{d}x' = \frac{\pi\widehat{\gamma}}{\sqrt{1+\widehat{\gamma}^2}}\arctan\left(\frac{\mathrm{i}+\widehat{\gamma}}{\sqrt{1+\widehat{\gamma}^2}}\right) - \widehat{\gamma}\int_0^{\pi/2}\frac{x'}{\mathrm{i}\sin(x')+\widehat{\gamma}}\mathrm{d}x',$$

which yields, to the leading order in $\widehat{\gamma}$,

$$\frac{2\widehat{\gamma}}{\sqrt{1+\widehat{\gamma}^2}}\int_0^{\pi/2}\arctan\left(\frac{\mathrm{i}+\widehat{\gamma}\tan(x'/2)}{\sqrt{1+\widehat{\gamma}^2}}\right)\mathrm{d}x' = \frac{\mathrm{i}\pi\widehat{\gamma}}{2\sqrt{1+\widehat{\gamma}^2}}\ln\left(\frac{2}{\widehat{\gamma}}\right) + \frac{\pi^2\widehat{\gamma}}{4\sqrt{1+\widehat{\gamma}^2}} + \frac{\mathrm{i}\widehat{\gamma}}{\sqrt{1+\widehat{\gamma}^2}}C_1 + O(\widehat{\gamma}^2\ln(\widehat{\gamma})) + O(\widehat{\gamma}^2),$$

where C_1 is equal to the convergent integral $2\int_0^1 \frac{\arctan(t)}{t}\,\mathrm{d}t$. Finally, we have:

$$\widetilde{\Phi}(\pi/2) = \eta\frac{\pi^2}{8} + \mathrm{i}\,C_1\frac{\widehat{\gamma}}{\sqrt{1+\widehat{\gamma}^2}} + O(\widehat{\gamma}^2\ln(\widehat{\gamma})) + O(\widehat{\gamma}^2) = \eta\frac{\pi^2}{8} + \mathrm{i}\,C_1\,\widehat{\gamma} + O(\widehat{\gamma}^2\ln(\widehat{\gamma})) + O(\widehat{\gamma}^2).$$

Similarly, one can show that :

$$\widetilde{\Phi}(-\pi/2) = \eta\frac{\pi^2}{8} - \mathrm{i}\,C_1\widehat{\gamma} + O(\widehat{\gamma}^2\ln(\widehat{\gamma})) + O(\widehat{\gamma}^2),$$

which ends the proof. ∎

Note that, to the leading order in $\widehat{\gamma}$, we find $\widetilde{\Phi}'(\pi/2) = \widetilde{\Phi}'(-\pi/2) = 0$ as we see on the sketch of the modulus of $\widetilde{\Psi}$ in figure 7.

Summary of the result. We now summarize the main result of the linear analysis. In the unstable regime of the Rayleigh equation (4.18) $(0 < K < 1)$ with periodic boundary conditions, and assuming that η and $\widehat{\gamma}$ are small parameters of the same order, we were able to find an approximate solution such that $\widehat{\gamma} = \eta$. This solution has boundary layers near $x = 0$ and $x = \pm\pi$ whose widths are of the order of $\widehat{\gamma} \approx \eta$. Reintroduction of the viscosity term, as in the original Eq. (4.17), only adds a small correction to this class of solutions as long as the viscosity is sufficiently small ($\epsilon/\eta^3 \ll 1$, based on a scaling analysis; see also remark 4.4 below). In the next subsection this finding is validated by numerical simulations.

4.1.1 Numerical validation of the analytic instability result

In this section, we validate the results obtained in the previous subsection. In order to do so, let us consider the following system:

$$\begin{cases} \partial_{t'}\widetilde{\omega} + \mathbf{u}\cdot\nabla\widetilde{\omega} = 0, \quad (t',\mathbf{x}) \in \mathbb{R}^+ \times (-\pi,\pi)\times\left(-\dfrac{\pi}{K},\dfrac{\pi}{K}\right), \\ -\Delta\widetilde{\Psi} = \widetilde{\omega}, \qquad \mathbf{u} = {}^{\perp}\nabla\widetilde{\Psi}, \quad (t',\mathbf{x}) \in \mathbb{R}^+ \times (-\pi,\pi)\times\left(-\dfrac{\pi}{K},\dfrac{\pi}{K}\right), \end{cases} \tag{4.31}$$

obtained from (4.14), by setting $\widetilde{\omega} = \omega - \omega_{eq}$, $\widetilde{\mathbf{u}} = \mathbf{u} - \mathbf{u}_{eq}$, and $\widetilde{\Psi} = \Psi - \Psi_{eq}$, and neglecting the viscous term (as we did in our analytical linear study). We solve (4.31) with the (DAMM)-scheme and we consider the following initial condition $\omega_{in}^D(x,y) = \cos(x) + \beta_1\cos(K\,y)$, with $\beta_1 = 1\times10^{-6}$. In the following, we consider two numerical tests.

Phase computation .

From Proposition 4.3, we have:

$$\theta_+ = \mathrm{Arctan}\left(\frac{C_1\,\widehat{\gamma}}{1+\frac{\pi^2\eta}{8}}\right) \approx \left(\frac{C_1\,\widehat{\gamma}}{1+\frac{\pi^2\eta}{8}}\right) := \vartheta. \tag{4.32}$$

Furthermore, we have $\widetilde{\Psi}(t',\pi/2,y) = \widehat{\Psi}(\pi/2)\,e^{\gamma t'}e^{\mathrm{i}Ky} = e^{\gamma t'}|\widehat{\Psi}(\pi/2)|\,e^{\mathrm{i}(Ky+\theta_+)}$. And then, for a fixed t', one has

$$\arg \max_{y\in[-\pi/K,\pi/K]} \mathcal{R}e\Big(\widetilde{\Psi}(t',\pi/2,y)\Big) := y_M = -\theta_+/K \approx -\vartheta/K\,.$$

This last relation allows us to validate numerically the linear instability result. Indeed, finding y_M numerically, we can compare the values of $K\,y_M$ with the analytical value of ϑ obtained from (4.32). In figure 8 (a), we plot the numerical as well as the analytical values of ϑ as a function of the aspect ratio $1/K$. We observe a good correspondence between the two curves, especially for small values of the aspect ratio. In figure 8 (b), the relative error between the values of ϑ obtained analytically and numerically is plotted. We remark that this error is mainly due to the error of the analytical estimate of the growth rate and increases with the aspect ratio. Indeed, we have proven that to the leading order, $\widehat{\gamma} = \eta$. But at the higher order, we have $\widehat{\gamma} = \eta + f(\eta)\,\eta^2$ where f is an unknown function satisfying $\lim_{\eta\to 0} f(\eta) < \infty$. Additional effects are: the truncation error of the numerical scheme (including the error caused by the stabilization parameter σ) and the error due to the determination of y_M. Indeed, the value of y_M is obtained numerically by finding the maximum of $\widetilde{\Psi}$ in y for $x = \pi/2$, an error of the order of Δy is then present for each point. To minimize this error, we took $N_y = 256$. Note that this error worsens when the aspect ratio increases, since L_y is proportional to this latter.

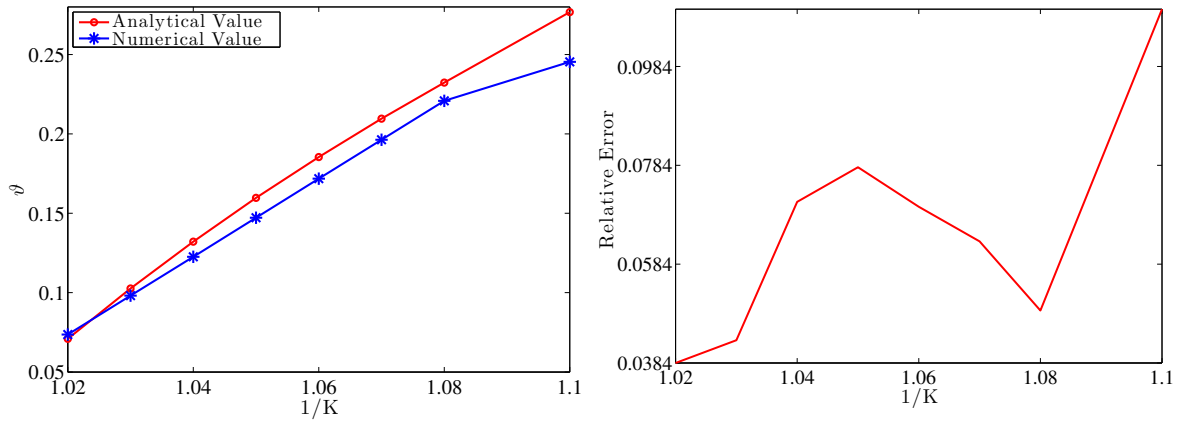

(a) (b)

Figure 8: (Kolmogorov case with initial condition ω_{in}^D). Evolution of the phase ϑ as a function of the aspect ratio $1/K$ (a), and relative errors between numerical and analytical values of the phase (b). Here, $N_x = N_y = 256$, $N_t = 200$, $\mathcal{T} = 20$, $\sigma = (\Delta x/L_x)^3$.

Growth rate.

In the linear phase, we have $\widetilde{\Psi}(t',x,y) = e^{\gamma t'}\,e^{\mathrm{i}Ky}\,\widehat{\Psi}(x)$. Thus,

$$\mathcal{S}(t) := \ln\Big(\|\widetilde{\Psi}(t,\cdot,\cdot)\|_{L^\infty(\Omega)}\Big) = \gamma\,t'. \tag{4.33}$$

In figure 9 (a), we plot the evolution of the value γ obtained numerically with the (DAMM)-scheme using (4.33) and the value of $K\eta$ for several values of the aspect ratio. As we observed for the phase computation, the comparison between the numerical value and the analytical one seems good, especially when the aspect ratio approaches 1. In figure 9 (b), the relative error between the analytical and the numerical values is plotted. Note that for values of the aspect ratio $1/K$ approaching 1, the relative error increases. This is due to the fact that in this limit, the boundary layer at $x = 0$ becomes sharp. The effect is therefore linked with the truncation error of the numerical scheme. For large values of η , the error is mainly due to the approximation $\widehat{\gamma} = \eta + f(\eta)\eta^2$ and it worsens when the aspect ratio increases. Nevertheless, the relative error remains limited and consistent with our analytical result.

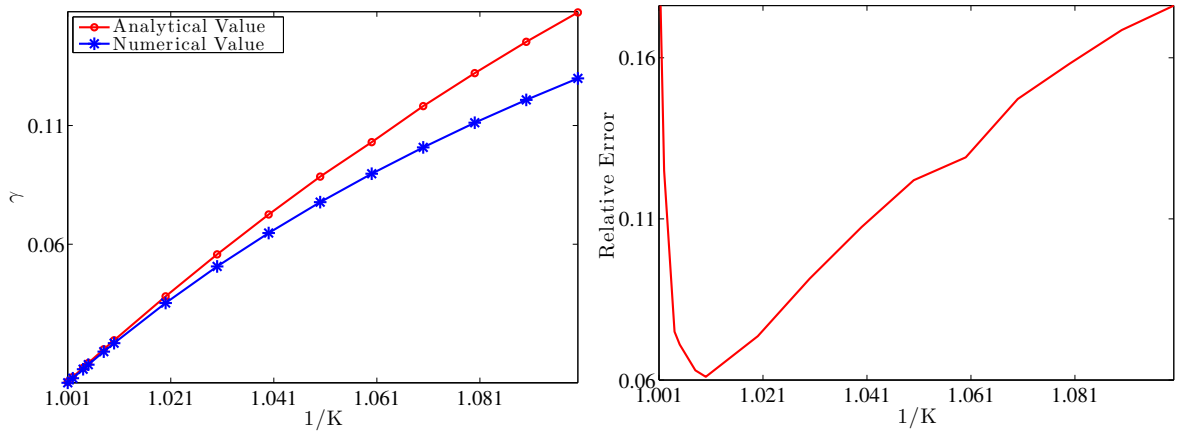

Figure 9: (Kolmogorov case with initial condition ω_{in}^{D}). Evolution of the growth rate γ as a function of the aspect ratio $1/K$ (a), and relative errors between numerical and analytical values of the growth rate (b). Here, $N_x = N_y = 128$, $N_t = 500$, $\mathcal{T} = 50$, $\sigma = (\Delta x/L_x)^3$.

Remark 4.2 *We recall that in order to obtain the equation* (4.18)*, we neglected the viscosity term. This approximation is valid when the viscosity* ϵ *verifies the following condition :* $\epsilon \ll \gamma\,\rho^2$ *, where* ρ *denotes the boundary layer thickness. Following our analysis, this condition becomes* $\epsilon \ll \eta^3$ *. Since* η *tends to* 0 *when the aspect ratio tends to* 1 *, we observe that the viscosity cannot be neglected in this limit. We can argue that for finite viscosity, the mode becomes stable if* $\eta \to 0$ *. This conclusion is consistent with the stability result obtained by [16], indicating that the instability region is attained for aspect ratio strictly superior to* 1 *for a finite value of viscosity .*

4.1.2 Digression: similarities and differences with tearing modes

At this point it is interesting to examine the analogy between the instability in the Kolmogorov flow and the tearing mode occurring in a magnetized plasma [8]. In the 2D MHD model with periodic boundary conditions [**?**, see for example]]phipsi, the equivalent of the equilibrium vorticity $\omega_{eq} = \cos(x)$ is an equilibrium current $J_{eq} = \cos(x)$ and its associated equilibrium magnetic flux function $\Psi_{eq} = \cos(x)$.

Carrying out a linear analysis similar to the one of the previous sections, one ends up with an outer equation for the perturbed flux function Ψ of the form

$$\sin(x)\,(\Psi''(x) + \eta\,\Psi(x)) = 0\,, \quad x \in (-\pi, \pi)\,. \tag{4.34}$$

This is reminiscent of equation (4.18), when the inertia term is ignored. One can then expect a linear mode structure similar to the one sketched in figure 7. The analogy however stops here. There is a fundamental difference between the instability of the Kolmogorov flow and the tearing mode instability which is the fact that the former exists in the ideal fluid (as shown in particular by the above analysis of the Rayleigh equation), whereas the latter requires dissipation. As it is known from the theory, the tearing mode growth rate scales like a fractional power of the resistivity (usually $\gamma \sim \eta^{3/5}$, for sufficiently small resistivity), which justifies neglecting the inertia in the limit of small resistivity. In the language of plasma physics this is called a *resistive instability*. Instead, we have seen that the Kolmogorov flow is unstable for arbitrarily small values of the viscosity provided that the aspect ratio exceeds unity, and that its growth rate depends only on a geometrical factor, the aspect ratio. Such a situation would be described as an *ideal instability* in the context of plasma physics.

This difference, resistive versus ideal instability, has a consequence on our understanding of the nonlinear phase of the instability. In the case of the tearing instability, an analytic theory for the nonlinear growth phase [19] and its saturation [6,17] could be developed by neglecting the plasma inertia. Instead, in the case of the instability of the Kolmogorov flow, no such theory exists, to our knowledge. One can however rely on numerical simulations. This is presented in the next sub-sections.

4.2 Kolmogorov flow : simulations of the instability

In this subsection we present results of the numerical simulations obtained with the (DAMM)-scheme of all the evolution regimes (linear, nonlinear and final) of the Kolmogorov flow, starting by perturbing an unstable steady state. Let us remark that for small perturbation amplitudes, the modes do not interact with each other (at least for some time) and the linear stability theory performed previously can be applied. As the perturbation grows, nonlinear terms become important, and mode-mode interactions eventually lead to the nonlinear saturation and a final non-trivial state.

Let $\Omega_S = (0, 2\pi) \times (0, 2\pi/K)$ and let us supply the system (2.11) with the initial condition $\omega^E_{in}(x, y) = \omega_{eq}(x) + \beta_3\,\mathcal{N}(x, y)$, where $\beta_3 = 0.01$ and $\mathcal{N}$ represents the noise introduced before. In this way, we perturb the steady-state solution of the Kolmogorov flow. We choose an aspect ratio of $1/K = 1.1$ and a viscosity of $\epsilon = 1 \times 10^{-3}$. The final physical time is $\mathcal{T} = 5000$. In figure 10, we plot the evolution of the vorticity $\omega^{\epsilon,\sigma}$ at different times, obtained with our (DAMM)-scheme. We observe again the formation of a variety of flow patterns. Starting from the initial condition (panel (a)), the first stage of the instability is clearly observable in panel (b). Then, we observe during a long time a complex behaviour characterized by the formation of the coherent structures embedded in a sea of filaments (panel (c) and (d)). And finally, in the long-time asymptotics, the vorticity begins to saturate (panel (e)), and a steady state constituted by a pair of opposed vortices is obtained (panel (f)). For this final state, the external

forcing term, which adds continuously kinetic energy to the system, is balanced by the viscous dissipation. Note that the wavy pattern obtained during the instability phase is very similar to the one obtained in the Taylor-Green instability (see figure 6).

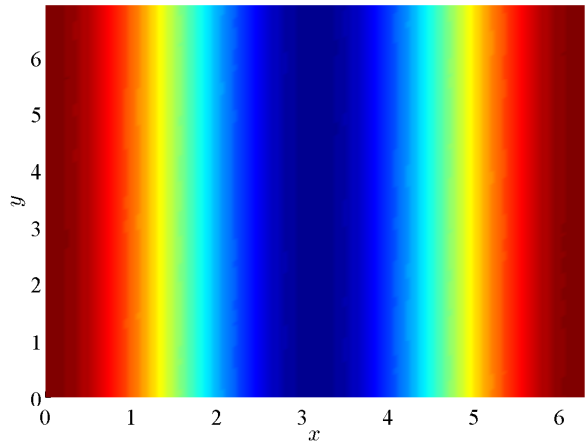

(a) (DAMM)-scheme, Initial condition .

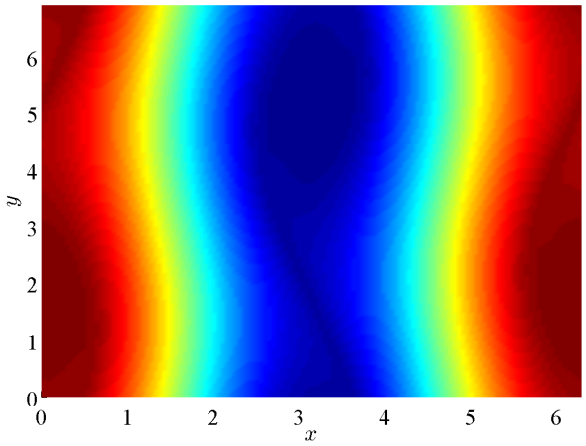

(b) (DAMM)-scheme, $t = 50$.

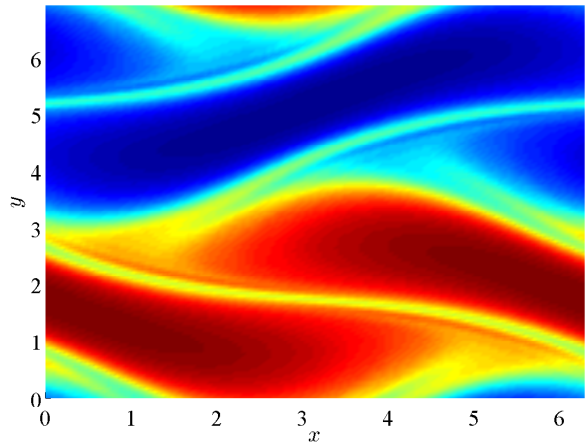

(c) (DAMM)-scheme, $t = 75$.

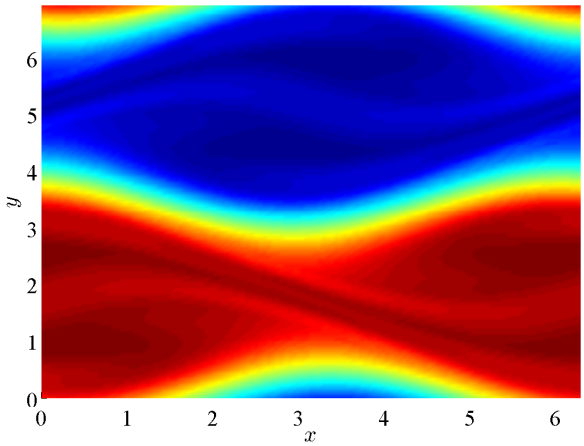

(d) (DAMM)-scheme, $t = 150$.

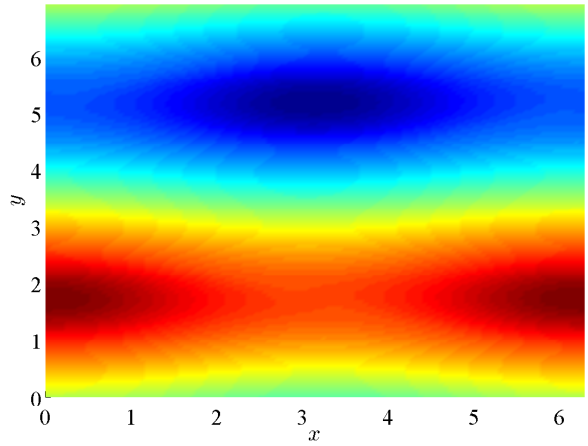

(e) (DAMM)-scheme, $t = 1000$.

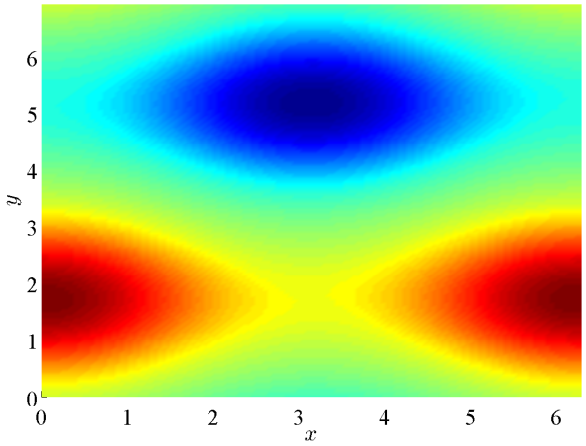

(f) (DAMM)-scheme, $t = 5000$.

Figure 10: (Kolmogorov flow with initial condition ω_{in}^{E}). Vorticity field $\omega^{\epsilon,\sigma}$ at different physical times, obtained with a viscosity of $\epsilon = 1e-3$. $N_x = N_y = 128$, $N_t = 50000$, $\mathcal{T} = 5000$, $\sigma = (\Delta x/L_x)^2$, and $K = 1/1.1$.

In order to understand in more details the Kolmogorov instability evolution, we

plot in figure 11 three panels corresponding to the evolution of the discrete L^∞-norm of $\widetilde{\Psi}$ in three adjacent time-intervals. Dividing the curve in three plots allows one to distinguish more clearly all phases of the instability process. In panel (a), we observe the events which occur at short times. The linear phase, characterized by the relation between the aspect ratio and the growth rate, appears first. A nonlinear stage follows immediately, characterized by a strong growth of the norm. This nonlinear phase continues in panel (b) but with a complete different evolution. After the growth of the norm in panel (a), we observe in panel (b) some damped oscillations and the decrease of the norm. This time-period corresponds to the merging and the filamentation of the vortices observed in figure 10. This oscillating phase is the most interesting one. Indeed, although the filamentation and the merging of the vortices lead to a very chaotic situation, the damped oscillations of the norm of $\widetilde{\Psi}$ seem to have more ordered variations. Finally, during the third and longest part of the instability, the norm in panel (c) continues to decrease but without any oscillation (or very weak oscillations impossible to see) before it saturates. This saturation phase means that the new equilibrium is attained.

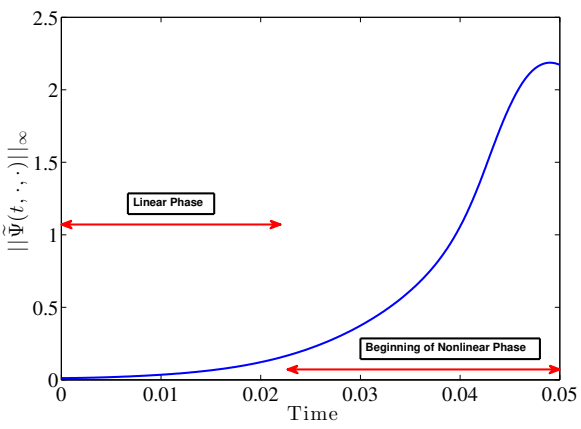

(a) $t' \in (0, 0.05)$.

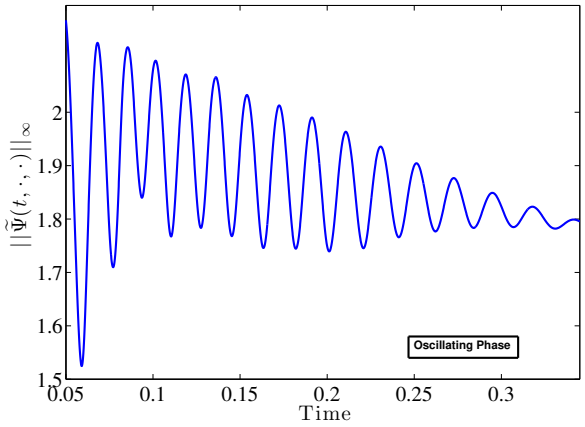

(b) $t' \in (0.05, 0.345)$.

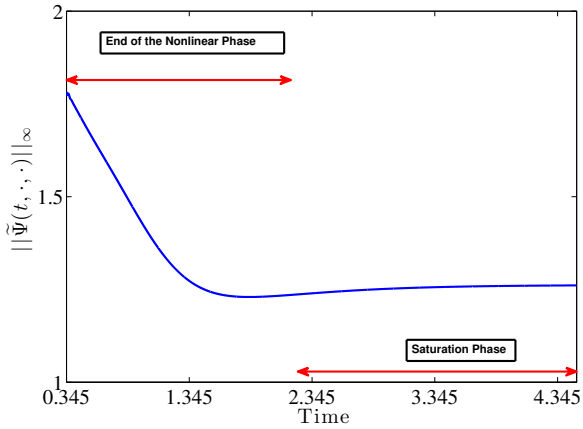

(c) $t' \in (0.345, 4.5)$.

Figure 11: (Kolmogorov flow with initial condition ω_{in}^{E}). Discrete L^{∞}-norm of $\widetilde{\Psi}$ versus time with $\epsilon = 1e-3$, $N_x = N_y = 64$, $N_t = 45000$, $\mathcal{T} = 4.5$, $\sigma = (\Delta x/L_x)^2$, and $K = 1/1.1$.

To end this section, we observe the relation between the vorticity and the stream function at the final time. Indeed, since the final pattern (panel (f)) in figure 10 does not evolve anymore, the Poisson bracket $\{\omega^{\epsilon,\sigma}, \Psi^{\epsilon,\sigma}\}$ should be of the same order as the term $\epsilon(\Delta\omega^{\epsilon,\sigma} + \cos(x))$. Since we have chosen $\epsilon = 1. \times 10^{-3}$, which is small, we should approach in this time asymptotic a functional relation between $\omega^{\epsilon,\sigma}$ and $\Psi^{\epsilon,\sigma}$. In figure 12 (a), we show the final state of the stream function $(-\Psi^{\epsilon,\sigma})$ corresponding to the vorticity field plotted in the figure 10 (panel (f)). As expected, we observe that the vorticity and the stream-function have very similar patterns, with the vorticity more concentrated at the extremal points of the field. In figure 12 (b), the $\omega^{\epsilon,\sigma} - \Psi^{\epsilon,\sigma}$-diagram at the final physical time $\mathcal{T}$ is shown. Despite an accumulation of points around the coordinates $(-0.25, 0.15)$ and $(0.25, -0.15)$, the vorticity and the stream-function seem to be linked with a *sinh* functional relation. We shall investigate in more details this point by studying the limit case $\epsilon \to 0$ in the next subsection.

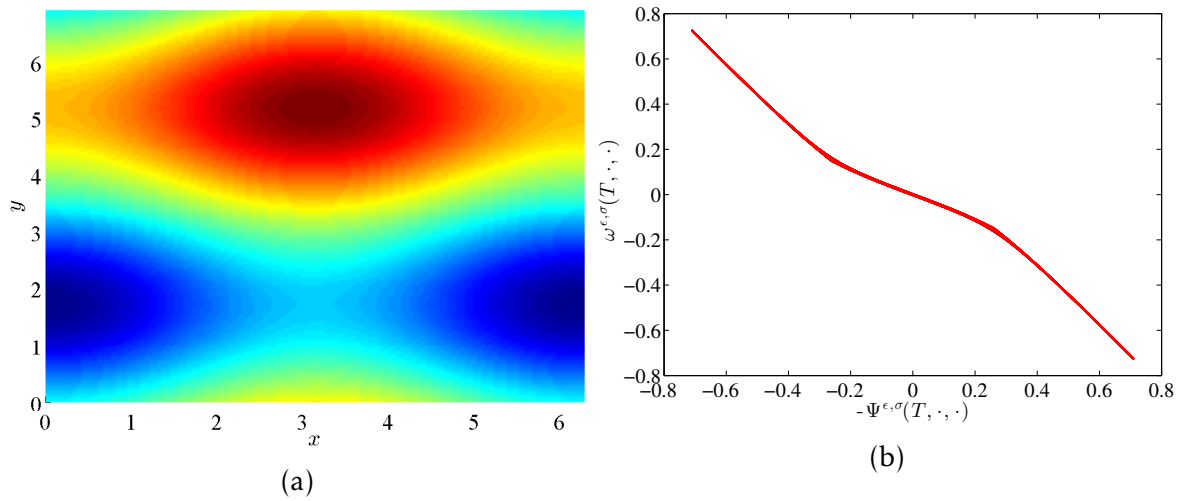

Figure 12: (Kolmogorov case with initial condition ω_{in}^{E}). Final state of the stream-function ($-\Psi^{\epsilon,\sigma}$) (panel (a)), and scatter plot between the vorticity and the stream function (panel (b)) obtained with a viscosity of $\epsilon = 1e-3$. $N_x = N_y = 128$, $N_t = 50000$, $\mathcal{T} = 5000$, $\sigma = (\Delta x/L_x)^2$, and $K = 1/1.1$.

4.3 Kolmogorov flow for vanishing values of ϵ

In this section, we consider $\epsilon = 0$ and the initial condition ω_{in}^{E}. In this limit, the physical time $\mathcal{T}$ tends to infinity. This allows one to study the long-time asymptotics of the flow. One of the strengths of the *Asymptotic-Preserving* properties of the (DAMM)-scheme is to allow attaining directly the equilibrium state without computing the intermediate states of the solution. Therefore, we take a large Δt, and obtain the final state without error accumulation. In figure 13, we plot the vorticity field $\omega^{0,\sigma}$ in the limit regime at the initial time $n = 0$ and at the final time step $n = 50$. We see that the pattern obtained in this way is very similar to the one obtained in the non-limit case (see figure 10 (f)). Note that the model that we study has symmetry translation in the y-direction. As a consequence, the final position of the vortices in the y-direction depends on the initial condition. In figure 14 (a), we have plotted the $\omega^{0,\sigma} - \Psi^{0,\sigma}$-diagram at the initial time. As expected, there is no functional relation between the two fields due to the noise introduced at this time. In figure 14 (b), the same $\omega^{0,\sigma} - \Psi^{0,\sigma}$ diagram is obtained after 50 time iterations, and we see the *sinh* functional relation already observed in the non-limit case (see figure 12 (b)). In order to validate our impression of a sinh-relation between $\omega^{0,\sigma}$ *and* $-\Psi^{0,\sigma}$, we plotted on the same figure 14 (b) a fitting function $f_{fit}(\cdot) = -a\sinh(b\,\cdot)$, with a and b two positive constants. The optimal values $a = 0.2255$ and $b = 2.7467$ were obtained by using an optimization Matlab tool. The fitting curve approaches well the numerical curve obtained with the (DAMM)-scheme. Keeping in mind that the limit stream function $\Psi^{0,\sigma}$ verifies the relation $-\Delta\Psi^{0,\sigma} = \omega^{0,\sigma} = -a\sinh(b\,\Psi^{0,\sigma})$, this allows one to find the form of the solution $\Psi^{0,\sigma}$. Indeed performing the following change of variables : $\Phi^{0,\sigma} = b\,\Psi^{0,\sigma}$, the function $\Phi^{0,\sigma}$ verifies then the *sinh*-relation $\Delta\Phi^{0,\sigma} = a\,b\sinh(\Phi^{0,\sigma})$. Inspired by the work of [9], where the previous sinh-Poisson relation is investigated,

we consider the following fitting solution Ψ_{fit} defined by

$$\Psi_{fit}(x,y) := \frac{4}{b}\tanh^{-1}\left(\frac{\sqrt{k}\,\mathrm{cn}(rx,k) - \sqrt{k_1}\,\mathrm{cn}(sy+\varphi,k_1)}{1+\sqrt{k\,k_1}\,\mathrm{cn}(rx,k)\,\mathrm{cn}(sy+\varphi,k_1)}\right),$$

where cn denotes the Jacobi elliptic function of the first kind, and $\varphi \in [0, 2\pi]$ to be fixed. Moreover, the parameters k, k_1, r and s verify the following system :

$$s^2(1-k_1)^2 = a\,b + 4\,r^2 k\,, \qquad s(1+k_1) = r(1+k)\,.$$

In order to close the system, we can remark that r and s are linked with the aspect ratio $1/K$, as well as the wave numbers k and k_1 thanks to the periodicity of the cn-function. We have then

$$2\,\pi\,r = 4\,I_J(k)\,, \qquad 2\,\pi\,s/K = 4\,I_J(k)\,,$$

where I_J denotes the complete Jacobi integral. From the value of $a\,b$ obtained from the fitting of the sinh relation, we are now able to resolve numerically the previous system in order to find the values of k, k_1, r and s. In figure 15, we plot in the panel (a) the stream-function obtained with the (DAMM)-scheme at the final time step, and in the panel (b) the steam-function obtained by fitting Ψ_{fit}. We have set $\varphi = 0.9$ in order to align the fitting solution with the numerical solution on the y-axis. Both plots are very similar.

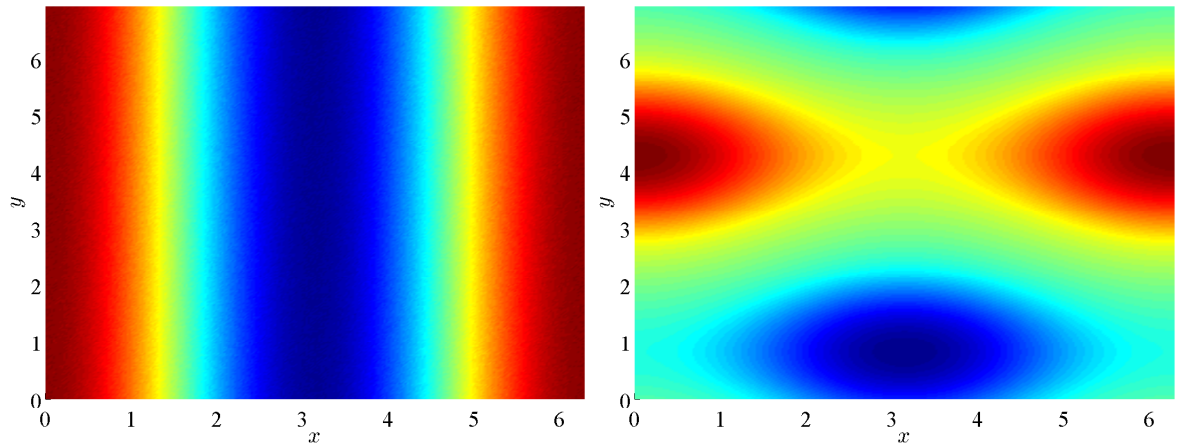

(a) (DAMM)-scheme, $n = 0$.

(b) (DAMM)-scheme, $n = N_t = 50$.

Figure 13: (Kolmogorov case for $\epsilon = 0$ with initial condition ω_{in}^{E}). Vorticity $\omega^{0,\sigma}$ at the initial time (panel (a)), and at the final time T (panel (b)). $N_x = N_y = 256$, $N_t = 50$, $T = 10$, $\sigma = (\Delta x/L_x)^2$, and $1/K = 1.1$.

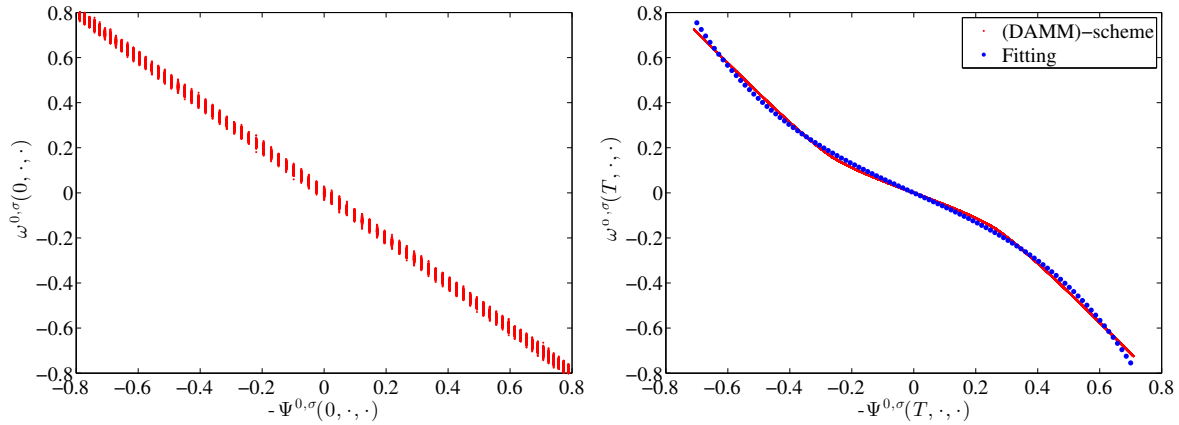

(a) (DAMM)-scheme, $n = 0$.

(b) (DAMM)-scheme, $n = 50$.

Figure 14: (Kolmogorov case for $\epsilon = 0$ with initial condition ω_{in}^{E}). Scatter plot between the vorticity and the stream function at the initial time (panel (a)) and at the final time (panel (b)). $N_x = N_y = 256$, $N_t = 50$, $T = 10$, $\sigma = (\Delta x/L_x)^2$, and $1/K = 1.1$.

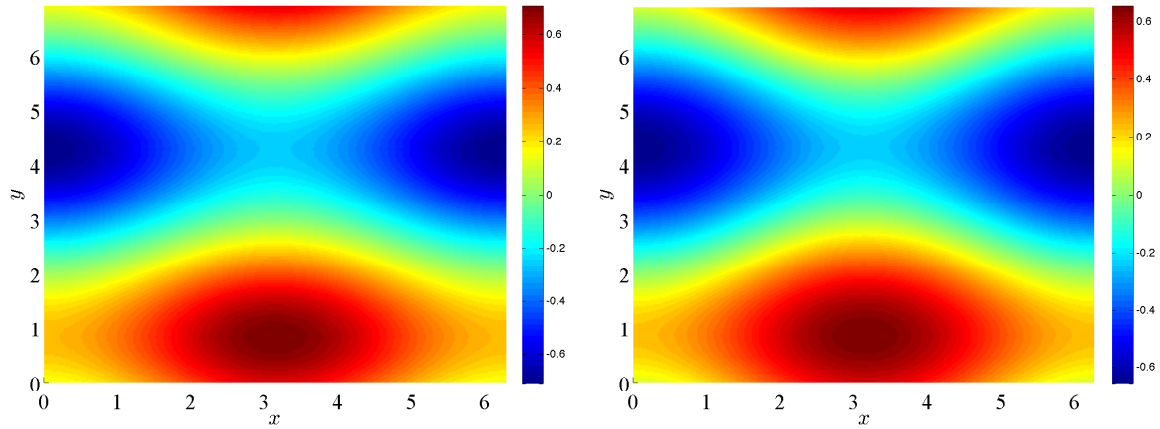

(a) (DAMM)-scheme, $n = N_t = 50$

(b) Fitting solution

Figure 15: (Kolmogorov case for $\epsilon = 0$ with initial condition ω_{in}^{E}). Stream function $(-\Psi^{0,\sigma})$ obtained with the (DAMM)-scheme (panel (a)) and with the fitting $(-\Psi_{fit})$ (panel (b)). $N_x = N_y = 256$, $N_t = 50$, $T = 10$, $\sigma = (\Delta x/L_x)^2$, and $1/K = 1.1$.

We conclude this section with a comparison between the results obtained with (DAMM)-scheme and with a standard pseudo-spectral code. Indeed the fact that Eq. (4.13) is implemented with periodic boundary conditions in a 2D-torus allows one to employ a truncated Fourier spectral representation of the vorticity. In Fourier space, the nonlinear terms are represented by a truncated convolution. This convolution is computed by using fast Fourier transforms to real space, so that products are computed locally at a given grid point, and transformed back to Fourier space (hence the term *pseudo-spectral*). In the code, an exact dealiasing technique based on staggered meshes is used [18]. Time advancing is explicit, employing a stabilized leap-frog scheme. In the context of this work, we call the scheme SER (spectral explicit reference) as it is used as a reference case to validate the (DAMM)-scheme in

the nonlinear regime where no exact solution is known.

In figure 16, we plot stream-function obtained with the (SER)-scheme at the physical time $t' = 5000$ for $\epsilon = 1\times10^{-3}$. With the exception of a translation along the y-axis (which is arbitrary, since the system is translationally invariant in y), the solutions obtained with both (DAMM) and (SER) schemes coincide (figure 12 (a)). In figure 17, we plot the $\omega - \Psi$ diagram as we did for the (DAMM)-scheme. The curve obtained is very similar to the one obtained with the (DAMM)-scheme (figure 12 (b)).

It is important to keep in mind that due to the explicit nature of the (SER)-scheme, it is not possible to work with arbitrarily small values of ϵ and to attain the late state directly. To give an idea, for the above simulations with the (SER)-scheme we had to use $N_t = 5 \times 10^6$ for $\epsilon = 1 \times 10^{-3}$) which corresponds to several viscous time scales, in order to achieve a the final state. This compares with a few tens of timesteps for a comparable result obtained with the (DAMM)-scheme, if one is interested only in the slow time scale dynamics.

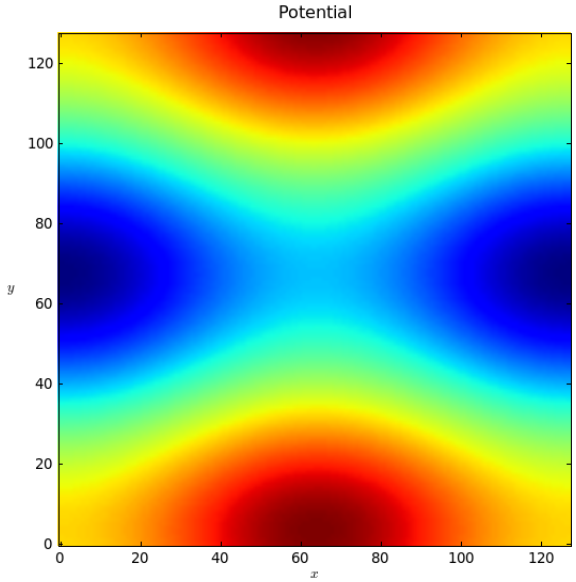

Figure 16: (Kolmogorov test case). Stream function ($-\Psi$) obtained with the SER-scheme at the final time $t' = \mathcal{T}$. Parameters were $N_x = N_y = 128$, $\Delta t = 0.001$, $\mathcal{T} = 5000$, $\epsilon = 1 \times 10^{-3}$ and $1/K = 1.1$.

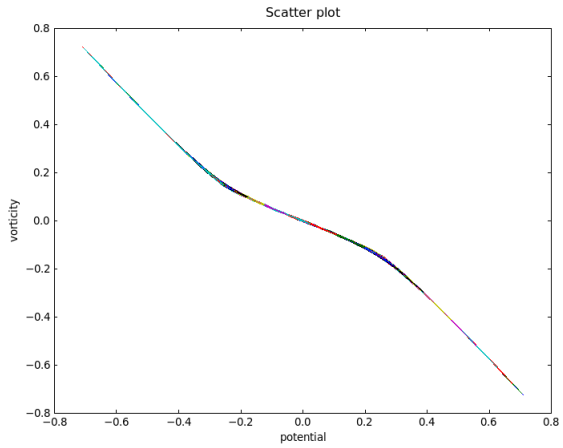

Figure 17: (Kolmogorov test case). Scatter plot between the vorticity and the stream function obtained with the SER-scheme at the time $t' = 10000$. Parameters were $N_x = N_y = 128$, $\Delta t = 0.001$, $\mathcal{T} = 10000$, $\epsilon = 1 \times 10^{-3}$ and $1/K = 1.1$.

5 Concluding remarks and perspectives

We now summarise the main aspects of this work

The main scope has been the development of an Asymptotic-Preserving scheme, referred here as (DAMM)-scheme, which simulates efficiently and accurately a variety of systems issued from fluid dynamics. The (DAMM)-scheme is constructed by combining a micro-macro decomposition with a regularization procedure. As a time integrator, the Diagonally Implicity Runge Kutta scheme provides the necessary good behaviour when working with large time steps.

As a test case system, we employed the 2D Navier-Stokes in two different set-ups, decaying Taylor-Green vortices and forced Kolmogorov flow. In particular, we have been able to show that the (DAMM)-scheme allows one to obtain very rapidly and accurately the late state of the unstable Kolmogorov flow, for any value of the small parameter, by fast-forwarding through the intermediate regime characterized by a shorter time scale.

This is made possible by a great strength of AP schemes, which is their capability of tuning the time step to the desired time scale. This is particularly clear from the study of the Kolmogorov flow, where the choice of a short time step allowed us to reproduce the linear growth, occurring on the inertial scale, whereas, by choosing a large time step proportional to the viscous time, we could obtain the final stationary state quite easily.

As a side result of the Kolmogorov flow study, we were able to identify a non-linear functional relation between vorticity and stream function which holds in the

final stable state and which appears to be universal. Further work is required to understand the origin of this relation, in terms, one can argue, of the stability properties of the final state.

Acknowledgments. This work has been carried out within the framework of the EUROfusion Consortium and has received funding from the Euratom research and training programme 2014-2018 and 2019-2020 under grant agreement No 633053. The views and opinions expressed herein do not necessarily reflect those of the European Commission.

Two of the authors (BF and MO) acknowledge the support of the French Agence Nationale de la Recherche (ANR) under grant ANR-MOONRISE.

References

[1] R. Alexander. Diagonally implicit runge-kutta methods for stiff o.d.e.'s. *SIAM Journal on Numerical Analysis*, 6:1006–1021, 1977.

[2] A. Arakawa. Computational design for long-term numerical integration of the equations of fluid motion: two dimensional incompressible flow. *Journal of Computational Physics*, 135:119–143, 1966.

[3] V. I. Arnol'd. Kolmogorov's hydrodynamic attractors. *Proc. Royal Soc. London A*, pages 19–22, 1991.

[4] V. I. Arnol'd and L. Meshalkin. Seminar led by an kolmogorov on selected problems of analysis. *Usp. Mat. Nauk*, 15:20–24, 1960.

[5] P. G. Drazin and W. H. Reid. *Hydrodynamic Stability*. Cambridge University Presse, 2nd Edition, 2010.

[6] D. Escande and M. Ottaviani. Simple and rigorous solution for the nonlinear tearing mode. *Phys. Letters*, 323:278–284, 2004.

[7] B. Fedele, C. Negulescu, and S. Possanner. Asymptotic-preserving scheme for the resolution of evolution equations stiff transport terms. *SIAM Multiscale Model. Simul.*, 17:307–343, 2019.

[8] H. Furth, J. Killeen, and M. N. Rosenbluth. Finite-resistivity instabilities of a sheet pinch. *Phys. Fluids*, 6:459–484, 1963.

[9] D. Gurarie and K. Chow. Vortex arrays for sinh-poisson equation of two-dimensional fluids : equilibria and stability. *Physics of fluids*, 16:3296–3305, 2004.

[10] A. Hasegawa and K. Mima. Stationary spectrum of strong turbulence in magnetized nonuniform plasma. *Phys. Rev. Letters*, 39:205–208, 1977.

[11] V. I.Yudovich. Example of the generation of a secondary stationary or periodic flow when there is loss of stability of the laminar flow of a viscous incompressible fluid. *Journal of Applied Mathematics and Mechanics*, 29:527–544, 1965.

[12] S. Jin. Efficient asymptotic-preserving schemes for some multiscale kinetic equations. *SIAM J. Sci. Comput.*, 21:441?454, 1999.

[13] A. Klar. An asymptotic-induced scheme for non-stationary transport equations in the diffusive limit. *SIAM Journal of Numerical Analysis*, 35:1073–1094, 1998.

[14] H. J. Lugt. *Vortex Flow in Nature and Technology*. John Wiley & Sons, 1983.

[15] C. Marchioro. An example of absence of turbulence for any reynolds number. *Commun. Math. Phys.*, 105:99–106, 1986.

[16] L. D. Meshalkin and I. G. Sinai. Investigation of the stability of a stationary solution of a system of equations for the plane movement of an incompressible viscous liquid. *PMM*, 6:1140–1143, 1961.

[17] F. Militello and F. Porcelli. Simple analysis of the nonlinear saturation of the tearing mode. *Phys. Plasmas*, 11:L13–L16, 2004.

[18] S. A. Orszag and G. S. Patterson. Spectral calculations of isotropic turbulence: Efficient removal of aliasing interactions. *Phys. Fluids*, 14:2538–2541, 1971.

[19] P. Rutherford. Nonlinear growth of the tearing mode. *Phys. Fluids*, 16:1903–1908, 1973.

[20] T. Sengupta, N. Sharma, and A. Sengupta. Non-linear instability analysis of the two-dimensional navier-stokes equation: the taylor-green vortex problem. *Physics of Fluids*, 30, 2018.

[21] D. Zwillinger. *Standard Mathematical Tables and Formulae*. CRC Press, 2012.